NTNU – Trondheim
Norwegian University of
Science and Technology

Optical Characterization of GaAs Nanowires Using Specular Mueller Matrix Ellipsometry

Christian Alexander Storås

Master of Science in Electronics
Submission date: July 2015
Supervisor: Helge Weman, IET
Co-supervisor: Morten Kildemo, Institutt for fysikk

Norwegian University of Science and Technology
Department of Electronics and Telecommunications

Master Thesis

Optical Characterization of GaAs Nanowires Using Specular Mueller Matrix Ellipsometry

by

Christian A. Storås

July 6, 2015

Supervisor: Professor Helge Weman, IET
Co-Supervisor: Professor Morten Kildemo, IFY

Dept. of Electronics and Telecommunication
Norwegian University of Science and Technology

Dedicated to my beloved father, mother and sister

Problem Description

Optical characterization of patterned surfaces consisting of GaAs nanowires using specular Mueller matrix ellipsometry and a regular unpolarised light scattering technique.

The project will aim at mapping out the complete polarimetric specular response of surfaces with GaAs nanowires including coated nanowires produced by a Molecular beam epitaxy. The photonic crystal consisting of regular patterns of cylinders will be studied in addition to randomly positioned nanowires. Wires of various height will also be studied.

The project is an experimental input to enable optical characterization of the dimension and average distance of the wires, in addition to lattice defects and possibly also detect the orientation of the hexagonal wire.

This experimental work will reveal the response that will be addressed in numerical work in a parallel project.

Abstract

The purpose of this thesis is to preform ellipsometric measurements to investigate the possibility of in situ characterization of nanowire growth. This will give an advantage for scientist in the future when growing nanowires both economic and time saving. Since ellipsometry is an accurate non-destructive technique, there are attractive possibilities for characterization of morphology and optical properties, which could lead to improving design of novel electro-optical devices. Seven different samples of nanowires were under investigation using specular Mueller matrix ellipsometry. The nanowires mainly consist of gallium arsenide (GaAs) grown on a Silicon (Si) substrate. Some core-shell structures was also investigated. The ellipsometric measurements have been done on both random and patterned grown nanowires, and characterized for different length and incidence angles. The patterned samples can be considered as photonic crystals, where the azimuthal orientation is displayed. There have previously been created a numerical algorithm to simulate Mie scattering for GaAs nanowires, as well as specular reflectance for an effective medium approximation looking at an ensemble of nanowires. For high density grown nanowires it is possible to detect similarities in behaviour between simulated and measured data for various incidence angles. It is possible to detect relatively high anisotropy in the measured Mueller matrix for the nanowire samples.

Sammendrag

Formålet med denne oppgaven er å utføre ellipsometri målinger for å etterforske muligheter for sanntid målinger ved groing av nanotråder. Dette kan gi store fordeler for forskere både økonomisk og tidsbesparende. Siden ellipsometri målinger er en nøyaktig og ikke ødeleggende teknikk, kan det benyttes for å karakterisere morfologi og optiske egenskaper til prøven, uten å ødelegge den. Dette kan være et nyttig verktøy til å forbedre elektro-optiske komponenter. Specular Mueller matrix ellipsometri har vært målt på syv forskjellig prøver med nanotåder. Nanotådene består av GaAs, grodd på Si substrate. Målingene har vært gjort for både mønstrede og umønstrede prøver, med ulike lengder. Ulike innfallsvinkler har vært undersøkt. For mønstrede prøver har også den asimutiske rotasjonen av prøven vært gransket. Tidligere har det vært laget en numerisk algoritme for simulering av Mie spredning på en nanotråd. Dette har så blitt utviklet videre til en effektiv medium modell for å se på en samling av nanotråder. Det er mulig å se likheter mellom simulert og målte data. Målinger viser også at prøvene består av relativ høy anisotropi.

Preface

The work in this thesis has been submitted as a partial fulfillment of the requirements for the degree of Master of science at the Norwegian University of Science and Technology (NTNU). The work is part of the research group to Professor Bjørn Ove Fimland and Professor Helge Weman, at department of Electronics and Telecommunications. Their research is about growth and characterization of nanowires. This thesis was supervised by Professor Helge Weman, while Professor Morten Kildemo served as co-supervisors.

I would like to express my gratitude to Professor Helge Weman for supervising my work and for giving me the opportunity to write my Master thesis for your research group. I would also thank my co-supervisor Professor Morten Kildemo for supervising me and for giving me the opportunity to work in his laboratory.

I would enlarge an especially thanks to system engineer Vedran Furtula, at departments of physics, for helping me with the instrument and helping me with the measurements for all the long hours in the lab. PhD candidate Dingding Ren has also been very helpful growing all the necessary samples and providing me with the corresponding SEM images.

I would also thank my family: my mother Ingri, my father Pål and my sister Madeleine for always believing in me, support me, and for giving me the best environment as possible during my entire education.

Thesis outline

This thesis consists of six parts: The introduction go through previous research and a short history section about the discovery of nanowires and ellipsometry. A background section give a superficial theory about the manufacturing method of the nanowires, including growth and patterning techniques, as well as substrate structure. A section of previous work is also included, which describe what the undersigned did in the project thesis. A theory section explain relevant theory, focusing on electromagnetic wave propagation. The experimental chapter explain the set up of the measurements, as well as the buildup of the software algorithm. The results and discussions focus on ellipsometric measurements and software simulations. A comparison of the software simulations with experimental measurements are discussed. A larger part will focus on the specular Mueller matrix measurements for investigating changes in behaviour for variation of incidence angles and azimuthal rotation of the samples. The nanostructures are either random grown or positioned in a hexagonal lattice.

Contents

Figures

Tables

1. Introduction

Nanostructures has become the new revolutionary method for semiconductor manufacturing. The fact that it is possible to fabricate and control small structures, thinner than a human hair, could potentially improve current technology and take it to a higher level. It is almost impossible to imagine what such structures can achieve inside different technological fields as for example in computer science, decreasing of energy consumption or medicine [3]. This chapter start with a short history of the nanowires before some potential applications are mentioned. Further a section of the history behind ellipsometry as well as different fields for characterization is presented. An overview over the rest of the thesis is presented, before the introduction end with some "crazy" ideas of problems super efficient solar cells could solve in the future.

1.1 Nanowires

Nanowires are anisotropic nanostructures with thickness many times smaller than length. They were first discovered by Wagner and Ellis in the 1960s [4], those were made of silicon (Si) and grown with a vapor-liquid-solid (VLS) mechanism. Since the discovery scientists have experimented with other materials and growth methods for producing new structures for new applications [5], [6]. Particularly have semiconductor nanowires grown from elemental groups: IV, II-VI and III-V been most investigated. Even though scientists have grown nanowires since the 60s, their optical properties are still not completely understood. Cao et al. [7], Bronstrup et al. [8] and Grzela [9] did characterization/simulation of scattering and absorption on Germanium (Ge), Silicon and Indium phosphide (InP) nanowires respectively. Even fewer have further extended the simulations of scattering and absorption into an effective medium model [10].

In recent years has the growth of nanowires attracted extra interest among scientists. Understanding the physics and chemistry behind these formations are essential for mapping out their functionality. Scientists have successfully manufactured several electro-optical applications of nanowires, such as lasers [11], light emitting diodes [12], [13], and solar cells [14], [15].

The nanowires under investigation in this thesis are intended to be used in solar cells. Research has already showed that nanowires increase the absorption of photons compared to thin film solar cells [16]. In these days where global warming is such a high issue, sun can be the new rescue for lowering the energy consumption of fossil fuels. If solar cells can be efficient enough, they can be imagined to become the revolutionary method for producing energy.

1.2 Ellipsometer

Just as important as the fabrication of nanostructures is the optical characterization of these formations. It would be impossible to make or improve a successful nanoscale devices without optical devices among them: Scanning electron microscope (SEM), Transmission electron microscopy (TEM) and Atomic force microscope (AFM). One of the latest inventions inside optical characterisation is the spectroscopic ellipsometry. Paul Drude can be looked as the inventor of ellipsometry. He derived the equations for Ψ and Δ, as well as reported the first experimental study [17]. The RC2 ellipsometer, which is the type used in this thesis, was first invented by Collins before it was further commercialized by J.A. Woollam Co. [18]. Ellipsometry is a very powerful technique due to the fact that it is nondestructive, nonintrusive and noninvasive. It is possible to measure optical dielectric constants and film thickness for material layers down to a size of 1 nm [18]. In the future ellipsometry can therefore compete with more conventional optical characterization devices for measuring sample properties.

With spectroscopic ellipsometry it is possible to characterize different types of samples, such as bulk materials, thin films and multilayered systems. This measurements give accurate characterization of surface roughness, interfaces and determination of the complex refractive index. Further information about fundamental physical properties such as morphology, crystallinity, chemical composition and electrical conductivity can be characterized [3], [19], [18]. The main advantage is the direct evaluation of the complex dielectric function ϵ. By only measuring the ellipsometric angles of Ψ and Δ it is possible to the derive the refractive index and the extinction coefficient [3]. A further explanation and derivation of Ψ and Δ follow in section 3.4.

Since the nanowires consist of geometric asymmetry ellipsometric measurements can give information about the effective dielectric constants and geometrical quantities. Even though ellipsometry measurements mainly have been used in thin film measurements it have been shown as a powerful technique to characterize anisotropic materials [20]. Recently have nanostructures been investigated with ellipsometry measurements: Oates et al. did ellipsometric characterization of silver nanorods, [21], [22], while Nerbø and Aas reported ellipsometric measurements on GaSb nanopillars [23], [24], [25]. Aas did also measurements on gold plasmonics [26] and Cu nanoparticles [27]. Fewer have reported ellipsometric measurements on nanowires.

Another powerful capability is the possibilities of in situ (real time) investigation. Ellipsometry is already used to determine film thickness for thin film growth and monitoring of etching depth [19], [18]. Even though no model exist for in situ characterization of nanostructures, such as nanowires. A model, monitoring real time growth would give huge advantages for scientist both economical and time saving.

1.3 Overview

This thesis is organised in 6 chapters, where chapter 2 gives a short introduction of growth techniques as well as previous work. Chapter 3 explain relevant theory. Further chapter 4 describe the buildup of the algorithm and the realization of the spectroscopic Mueller matrix measurements. Before results of the simulation and measurements are listed, followed by comparison and discussion in chapter 5. In the conclusions an overview of the

most important results and outlook are summarized.

1.4 Solar cells in the future

With improved super efficient solar cells only fantasy can limit the field of use. With solar cells we could imagine a zero-emission society and global warming will never more become an issue. In the future even cars, trains and airplanes could run on solar energy. Not only preventing global warming but could also be significant for other applications. For example could we imagine the cover of the cell phones to be composed of solar cells, so the battery could be charged when the phone lay in the sun. One of the main issues for speed limits on the Japanese bullet train Shinkansen is the overhead power supply wire. This wire gives limitation to the speed limit of the train, due to friction and wear. If the train ran on solar energy this would no longer be an issue and these trains could travel even faster. Engine fail out due to lack of gasoline have caused many airplanes to crash, like Air Canada flight 143, Air Transat flight 236 and British Airways flight 38. These incidences could all be avoided if the engines were supplied with solar energy from attached solar cells on top of the fuselage. But the first step for make all these technologies possible is to map out and understand the properties of some small components inside a solar cell; called nanowires.

2. Background

Norwegian university of science and technology (NTNU) started to grow nanowires in 2006 with a Molecular beam Epitaxy (MBE), using a vapor liquid solid (VLS) growth method. This chapter will provide a short introduction and theory for different techniques applied for nanowire growth, as well as previous work. Since this thesis is all about characterization of nanowires, and do not consist of any growth work, will therefore this part be short and superficial.

2.1 Manufacturing method

All the nanowire samples in this thesis was epitaxialy grown with a Molecular beam epitaxy (MBE). The nanowires can either be arranged random or position oriented. In the case of position growth nanowires, a patterning technique leave holes on the substrate at desired locations. Thereafter the nanowires are grown inside the MBE chamber, where the molecules will diffuse into these holes and build up layer by layer until they become nanowires. There exist several techniques for manipulating the growth of the nanowires into desired pattern. The pattern techniques utilized in this thesis was either electron beam lithography or nanoimprint lithography.

2.1.1 Molecular beam epitaxy (MBE)

Molecular beam epitaxy is an epitaxial growth technique for depositing a layer of a material on a crystalline substrate, like silicon (Si). The primary material deposited on this crystalline substrate is GaAs, but can also be any other types of III-V semiconductors. The substrate is placed in a chamber with ultra high vacuum. The source material is evaporated and fired against the substrate, by an electron gun. After hitting the substrate the material is absorbed onto the surface, due to surface diffusion, the molecules move until they find their energetically favorable location at the substrate, depending on the crystal structure. It is possible to control the growth by building up ultra thin layers of the evaporated material. By manipulating the atoms correctly, it is possible to grow different kind of nanostructures like nanowires [1]. Epitaxial growth is the only growth technique which gives high quality nanostructures on crystalline material for many semiconductor materials.

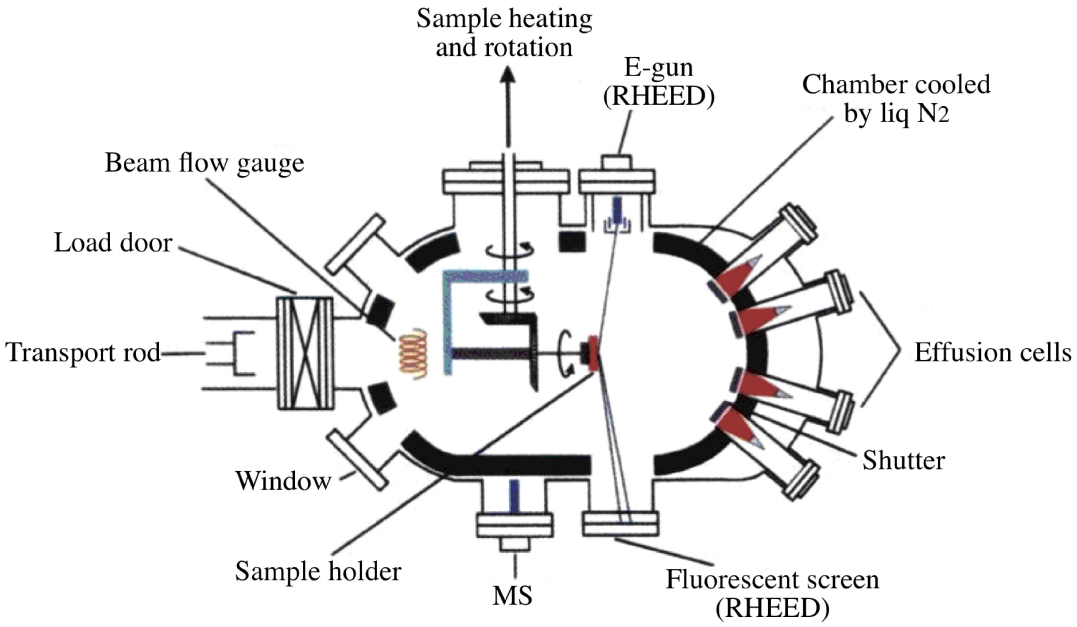

Figure 2.1: A sketch of a typical Molecular beam epitaxy chamber, with associated labeled components. The figure is taken from cnx.org [1].

2.1.2 Electron beam lithography (EBL)

Electron beam lithography is a direct-write method for designing specific patterns on a desirable sample. An electron gun accelerate and focus a beam of electrons against a sample surface. Depending on the EBL device the beam is focused magnetically or electrostatically. The technique is modified from a scanning electron microscope, and therefore give possibilities to control high resolution patterns on the surface. Before the scanning procedure begins the sample is coated with a photoresist film. After the electron gun have scanned across the resist covered sample an etching process remove the resist and leave a desired pattern on the sample. There are though some advantages and disadvantages using an EBL technique: It gives very high resolution, only limited by electron scattering and can be used on a high variety of materials, but it is slow compared to optical lithography, and it is also very expensive [28].

2.1.3 Nanoimprint lithography (NIL)

Nanoimprint lithography consist of two basic steps: A mold is pressed into a resist on top of a substrate. The resist is heated up to its glass transition temperature so the mold shape should easier be imprinted onto the resist. When the mold is removed a pattern is left on the resist. An etching process transfer the pattern onto the substrate. Since nanoimprint lithography does not use any energetic beam, it has several advantages compared to EBL, such as no limitation due to electron scattering. NIL is also a faster and more economical technique than EBL. It is therefore used in mass production of nanostructures [29].

Figure 2.2: A picture of an Electron beam lithography equipment similar the one equipped at NTNU-nanolab [2].

2.2 Nanowires and substrate structure

This thesis include characterization on different nanowires, primary consisting of GaAs with different length and pattern. The nanowires were grown on p-type Silicon (111) substrate, where the nanowires were grown along the [111]B direction, with homogeneous diameters. On top of the Silicon substrate there is a thin layer of Silicon-oxide. For the simulation, this oxide layer is disregarded, since it is very thin compared to the substrate thickness and the length of the nanowires. There have been done measurements on both patterned and random growth samples. The patterned samples are regarded as photonic crystals. The nanowires are grown with a VLS method, with a droplet on top of each wire. Surface roughness can be observed in scanning electron microscopy (SEM) images. The light scattering and the reduction in specular reflectance depends on this surface roughness, which is not included in the software simulations.

2.3 Previous work

Previously there has been created a software algorithm for simulation of scattering and absorption looking at one single nanowire. Some results from this work have been included in section 5.1.1, since it is important for further calculations. The far field Mie scattering for one nanowires was later extended in an effective medium approximation, where we look at an ensemble of nanowires, shown in section 5.1.2. The measurements was either compared with scientific papers or experimental measurements to validate the authenticity of the algorithm. The effective medium approximation did not work quiet well, and some small corrections in the algorithm were applied later.

3. Theory

This chapter contain some background theory essential for understanding the principles behind ellipsometry and for simulations of scattering and absorption on nanowires. The chapter begin with the cornerstones in electromagnetic theory: Maxwell's equations, and further explain wave propagation and polarisation from these equations. The infinite series of the scattering coefficient and effective medium theory will also be explained, as well as theory behind ellipsometry. The major part of the electromagnetic wave propagation theory are explained more thoroughly in Bohren and Huffman [30], while theory about ellipsometry can be found in Fujiwara [19] and the handbook of ellipsometry [18].

3.1 Fundamental electromagnetic theory

Light can either be described as waves or electromagnetic particles, also known as photons. These particles travel in an electromagnetic field consisting of both an electric component and a magnetic component. When light propagate into an obstacle the electromagnetic fields change behaviour, this is significant for the understanding and discovery of ellipsometry, but also fundamental for the software program created in this thesis. For understanding the mechanism behind light interaction between an obstacle and the ambient medium the electromagnetic fields have to be investigated, starting with Maxwell's equations.

3.1.1 Maxwell's equations

Maxwell equations are the fundamental equations for describing the properties of electromagnetic waves:

$$\begin{aligned} &\nabla \cdot \mathbf{D} = \rho_f, \\ &\nabla \times \mathbf{E} + \tfrac{\partial \mathbf{B}}{\partial t} = 0, \\ &\nabla \cdot \mathbf{B} = 0, \\ &\nabla \times \mathbf{H} = \mathbf{J_f} + \tfrac{\partial \mathbf{D}}{\partial t}, \end{aligned} \tag{3.1}$$

where $\mathbf{E}$ is the electric field and $\mathbf{B}$ is the magnetic induction. A relation between the magnetic field $\mathbf{H}$ and $\mathbf{B}$, and a relation between the electric displacement $\mathbf{D}$ and $\mathbf{E}$ are defined in equation (3.2).

$$\begin{aligned} \mathbf{D} &= \epsilon_0 \mathbf{E} + \mathbf{P}, \\ \mathbf{H} &= \tfrac{\mathbf{B}}{\mu_0} - \mathbf{M}. \end{aligned} \tag{3.2}$$

$\mathbf{P}$ is a notation for the electric polarization defined as the average dipole moment per unit volume and $\mathbf{M}$ is the magnetization defined as the average magnetic dipole moment per

unit volume. ϵ_0 and μ_0 are the permittivity and permeability for light travelling in vacuum. ρ_f is the charge density and $\mathbf{J_f}$ is the current density in free charges.

A relation between the electric and the magnetic fields are shown in equation (3.3).

$$\begin{aligned} \mathbf{J_f} &= \sigma \mathbf{E}, \\ \mathbf{B} &= \mu \mathbf{H}, \\ \mathbf{P} &= \epsilon_0 \chi \mathbf{E}, \end{aligned} \tag{3.3}$$

where σ is the conductivity, μ permeability and χ the electric susceptibility. The coefficients are assumed to be linear, homogeneous and isotropic in the medium.

3.1.2 Wave propagation in an arbitrary particle

When an electromagnetic wave interact with an arbitrary particle, consisting of a different material as the surrounding medium, an interaction on the electromagnetic wave will occur. Electric charges in the wave start to oscillate in the particle, and the electromagnetic energy will reradiate in all directions. The characteristics of a wave propagated through an arbitrary particle are determined by the amount of light scattered and absorbed in the particle (scattering and absorption will be described more thoroughly in section 3.7). Depending on the particles geometry (e.g. shape and size) and material (e.g. refractive index) the amount of scattered and absorbed light alter. Figure 3.1 show a sketch of an arbitrary particle, where (E_p, H_p) are defined as the electromagnetic fields inside the particle, (E_m, H_m) are the electromagnetic fields in the ambient medium, surrounding the particle, while (E_s, H_s) are the scattered fields and (E_i, H_i) are the incoming incident fields illuminated by and incident wave.

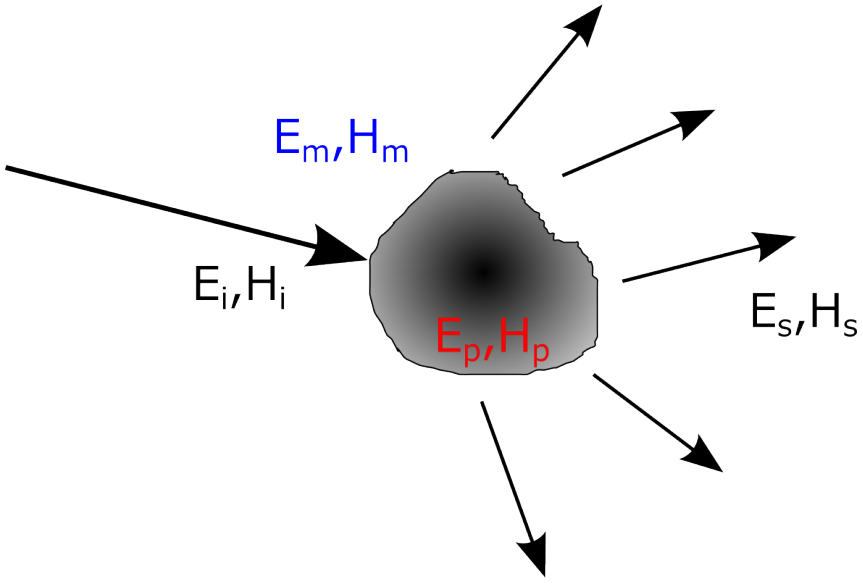

Figure 3.1: A sketch of an incident plane wave (E_i, H_i), propagating into an arbitrary particle with scattered electromagnetic fields (E_s, H_s). (E_m, H_m) and (E_p, H_p) are the electromagnetic fields in the ambient medium and the particle respectively.

By assuming the incident light to be plane harmonic waves with electric field: $\mathbf{E_i} = \mathbf{E_0} e^{i\mathbf{k}\cdot\mathbf{z} - i\omega t}$, and magnetic field: $\mathbf{H_i} = \mathbf{H_0} e^{i\mathbf{k}\cdot\mathbf{z} - i\omega t}$, where we assume propagation in z-direction for a certain time t, with a wave number k and an angular frequency ω. The

electromagnetic fields in the surrounding medium can be expressed as a superposition between the incident and the scattered fields:

$$\begin{aligned} \mathbf{E_m} &= \mathbf{E_i} + \mathbf{E_s}, \\ \mathbf{H_m} &= \mathbf{H_i} + \mathbf{H_s}. \end{aligned} \tag{3.4}$$

Maxwell's equations will always be satisfied for plane harmonic waves with continues ϵ and μ. From the classical Maxwell's equations (3.1) it is possible to derive the plane harmonic Maxwell equations:

$$\begin{aligned} &\nabla \cdot \mathbf{E} = 0, \\ &\nabla \times \mathbf{E} = i\omega\mu\mathbf{H}, \\ &\nabla \cdot \mathbf{H} = 0, \\ &\nabla \times \mathbf{H} = -i\omega\epsilon\mathbf{E}. \end{aligned} \tag{3.5}$$

By using equation (3.5) and the vector identity: $\nabla \times (\nabla \times \mathbf{A}) = \nabla(\nabla \cdot \mathbf{A}) - \nabla \cdot (\nabla \mathbf{A})$ and change the arbitrary vector field $\mathbf{A}$ with the electromagnetic fields for the electric and the magnetic field components, it is possible to derive the plane harmonic wave equation:

$$\begin{aligned} \nabla^2\mathbf{E} + k^2\mathbf{E} = 0, \\ \nabla^2\mathbf{H} + k^2\mathbf{H} = 0. \end{aligned} \tag{3.6}$$

Simple algebra can easy show that the the wave vector k, in equation (3.6), can be defined as: $k^2 = \omega^2\epsilon\mu$.

3.1.3 Boundary conditions

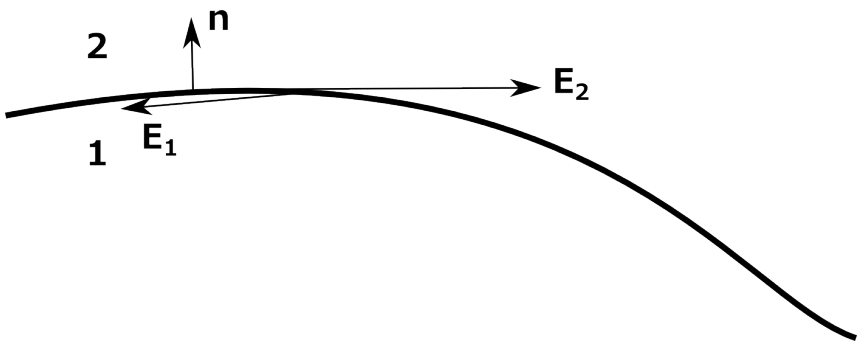

Figure 3.2: A sketch of the electric field between the boundary of two mediums; 1 and 2, corresponding to equation (3.7). **n** is the normal vector pointing out of the boundary.

When light propagates into a boundary between two different mediums the permittivity ϵ and the permeability μ are no longer continues. Therefore it is necessary to define a relation between the electric fields and the magnetic fields at the boundary between those two mediums, given in equation (3.7). The displacement and the magnetic induction relations lays normal to the tangential plane, while the electric field and the magnetic field relation acts parallel with the boundary.

$$
\begin{aligned}
&[\mathbf{E_2}(\mathbf{x}) - \mathbf{E_1}(\mathbf{x})] \times \hat{\mathbf{n}} = 0, \\
&[\mathbf{H_2}(\mathbf{x}) - \mathbf{H_1}(\mathbf{x})] \times \hat{\mathbf{n}} = J_s, \\
&[\mathbf{D_2}(\mathbf{x}) - \mathbf{D_1}(\mathbf{x})] \cdot \hat{\mathbf{n}} = \rho_s, \\
&[\mathbf{B_2}(\mathbf{x}) - \mathbf{B_1}(\mathbf{x})] \cdot \hat{\mathbf{n}} = 0.
\end{aligned}
\tag{3.7}
$$

It can be proved that the tangential component of $\mathbf{E}$, and the normal component of $\mathbf{B}$ are continues across the boundary. If there is no surface charge ρ_s and no surface current density J_s the tangential $\mathbf{H}$ component and the normal component of $\mathbf{D}$ can also be proved to be continues across the boundary. Some calculations and argumentation for conservation of energy can prove that the electromagnetic fields are continues across the boundary. Figure 3.2 illustrates the electric fields for a wave propagating in a certain direction along the surface boundary, where $\hat{n}$ is the normal vector pointing out of the surface.

3.1.4 Poynting vector

The Poynting vector: $\mathbf{S} = \mathbf{E} \times \mathbf{H}$ express the transferred electromagnetic energy at all points in an area. The most ordinary form of Poynting vector is the time-averaged, which are used in harmonic fields:

$$
< \mathbf{S} >= \frac{1}{2} Re\{E_c \times H_c^*\}. \tag{3.8}
$$

3.2 Refractive index

The refractive index n, is a measure of the delay of light propagating in a specific medium compared to light propagation in vacuum. The refractive index is defined as $n = \frac{c}{v}$, where c is the speed of light in vacuum and v the velocity in the medium ($v = \frac{\omega}{k}$). When a light wave propagate into a boundary between two mediums, some of the light will be transmitted through the boundary and some will be reflected. Snell's law and Fresnel equations describe the amount of light which undergo these two processes. Therefore it is possible to calculate the refractive index in the particle through a relation between the transmitted and reflected angles.

The refractive index can also be defined as a combination of the permittivity (ϵ_r) and permeability (μ_r) in the medium: $n = \sqrt{\epsilon_r \mu_r} \approx \sqrt{\epsilon_r}$, since μ_r is close to one for almost all materials. A dielectric tensor can therefore be defined for a cartesian coordinate system, which describes the anisotropy of a particle:

$$
\epsilon_r = \begin{pmatrix} \epsilon_{xx} & \epsilon_{xy} & \epsilon_{xz} \\ \epsilon_{yx} & \epsilon_{yy} & \epsilon_{yz} \\ \epsilon_{zx} & \epsilon_{zy} & \epsilon_{zz} \end{pmatrix}. \tag{3.9}
$$

In fact it is possible to rotate this tensor in an arbitrary direction, for a suitable geometry with axes (ξ, η, ζ) by using the Euler rotation formula [31]:

$$
\epsilon(x, y, z) = \mathbf{A}(\phi, \theta, \psi)\epsilon(\xi, \eta, \zeta)\mathbf{A}(-\phi, -\theta, -\psi). \tag{3.10}
$$

The matrix **A** is given in Goldstein et al. [31]. By using correct angles between the particle axes (ξ, η, ζ) and the reference axes (x, y, z), and symmetry. It is nearly always possible to write the dielectric tensor as a diagonal tensor:

$$\epsilon_r = \begin{pmatrix} \epsilon_\xi & 0 & 0 \\ 0 & \epsilon_\eta & 0 \\ 0 & 0 & \epsilon_\zeta \end{pmatrix}. \tag{3.11}$$

3.2.1 Effective refractive index

Effective refractive index N_{eff} is a measure of the overall delay for the propagating wave in a medium. For our case nanowires lying on top of a substrate, where it is possible to introduce an effective refractive index in the surrounding inhomogeneous medium.

Van Hulst [32] derive an expression of the effective refractive index:

$$N_{eff,p,s} = 1 - i\mathbf{S_{p,s}} \cdot 2\pi N k^{-3}. \tag{3.12}$$

$\mathbf{S_{p,s}}(\mathbf{0})$ denotes the scattering field for p- and s-polarised light respectively. k is the wave vector and N is the amount of particles per unit volume. If the real and the imaginary part of the scattering field is separated, equation (3.12) describes two effects:

$$N_{eff,p,s} = n_{eff,p,s} - ik_{eff,p,s}, \tag{3.13}$$

$$n_{eff,p,s} = 1 + 2\pi N k^{-3} Im\{\mathbf{S_{p,s}}\}, \tag{3.14}$$

$$k_{eff,p,s} = 2\pi N k^{-3} Re\{\mathbf{S_{p,s}}\}. \tag{3.15}$$

The real part of the effective refractive index, equation (3.14), determines a phase shift of the wave propagating in the medium, also known as dispersion, while the imaginary part, equation (3.15), tell something about the attenuation of the intensity. The phase velocity in the medium is now changed to $c = \frac{c_0}{n_{eff,p,s}}$.

3.3 Polarisation

A propagating monochromatic electromagnetic wave consist of both an electric and a magnetic field oscillating either parallel or perpendicular along the propagating wave. There are two notations mainly used for defining polarised light: TE and TM or s- and p-polarised. If the electric field propagates as a transversed wave, the wave is said to be TE-polarised, while if the magnetic field propagates as a transversed wave, the wave is said to be TM-polarised. P- and s-polarised light is defined by the oscillation of the electric field. If the electric field oscillates in parallel to the propagating wave, the wave is said to be p-polarised, while if the electric field oscillates perpendicular to the wave it is said to be s-polarised. In other words a TE-polarised wave and a s-polarised wave are identical, while a TM-polarised wave is equal to a p-polarised wave. An overview over the p- and s-polarised convention is shown i Figure 3.3.

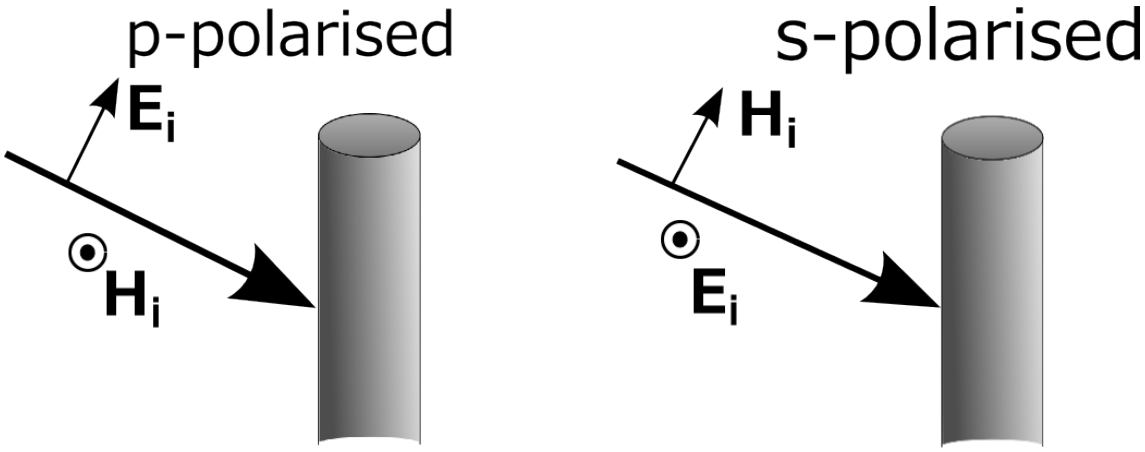

Figure 3.3: A sketch of the orientation to the electromagnetic fields for a p-polarised and a s-polarised incident wave. For example the electric field can either oscillate in the plane with the cylinder axis or perpendicular to this plane. The same applies for the magnetic field.

An electromagnetic wave can also be described through three different types of polarisation shapes depending on the form of the oscillations to the electric and magnetic components: Linear, circular or elliptical. Elliptical and circular (which is a special case of an ellipse) polarised light are said to either be oriented clockwise (right handed) or counterclockwise (left handed). If we imagine polarised light, linear or elliptical, propagating in a given direction into a particle. Observed changes in the real part of the refractive index would indicate a briefringent medium, while changes in the imaginary part indicate a dichroic medium.

If the light source emit light in a polarisation, which have not a well defined shape (the polarisation shape is not linear, circular or elliptical). This type of light is said to be unpolarised. The majority of natural light is normally not polarised.

3.3.1 Jones vector

Polarisation describe the orientation in space for a propagating electromagnetic wave, usually expressed in a cartesian coordinate system as a time dependent harmonic field travelling in $\hat{z}$-direction. $\hat{x}$ and $\hat{y}$ express a superposition of the oscillating electric field:

$$\mathbf{E(z,t)} = \mathbf{E_{0x}} e^{\mathbf{i}(\omega \mathbf{t} - \mathbf{2}\pi \mathbf{z}/\lambda + \phi_\mathbf{x})} \hat{\mathbf{x}} + \mathbf{E_{0y}} e^{\mathbf{i}(\omega \mathbf{t} - \mathbf{2}\pi \mathbf{z}/\lambda + \phi_\mathbf{y})} \hat{\mathbf{y}}, \tag{3.16}$$

where λ is the wavelength, ω the angular frequency and ϕ a phase shift. In general are there the amplitudes E_{0x} and E_{0y} and the phase difference between these two components: $\phi = \phi_x - \phi_y$, which determine the shape of the polarisation. The magnetic field component is typically disregarded due to $\mu_r \approx 1$ for most materials. Commonly we express the polarisation state of this arbitrary wave as a Jones vector:

$$\mathbf{J} = \begin{bmatrix} E_x \\ E_y \end{bmatrix} = \begin{bmatrix} E_{0x} e^{i\phi_x} \\ E_{0y} e^{i\phi_y} \end{bmatrix}. \tag{3.17}$$

When the light wave interact with another material a change in polarisation may occur due to reflection and transmission properties in the material. A Jones transferring matrix **J** describe the interaction between the incoming polarised wave and the outgoing:

$$J_{out} = \mathbf{J} \cdot J_{in}, \tag{3.18}$$

$$\mathbf{J} = \begin{bmatrix} a & b \\ c & d \end{bmatrix}, \tag{3.19}$$

where the letters a, b, c and d, in Jones transfer matrix equation (3.19), define the complex transmission or reflection coefficients. Note that the Jones vector conversion is only valid for fully polarised light.

3.3.2 Stokes parameters

Sometimes light is quasi-monochromatic, which means the light do not necessary need to be a time harmonic monochromatic wave, but may have a finite band width and time dependent electric field for the amplitudes and phases. Due to this time dependency the Jones vector is also time dependent. This makes the Jones vector complex, and therefore the Mueller-Stoke formalism was invented. By define the polarisation through intensities and take the time average of the electric field the Stokes parameters are defined:

$$\mathbf{S} = \begin{bmatrix} s_1 \\ s_2 \\ s_3 \\ s_4 \end{bmatrix} = \begin{bmatrix} I \\ Q \\ U \\ V \end{bmatrix} = \begin{bmatrix} I_x + I_y \\ I_x - I_y \\ I_{+45^\circ} - I_{-45^\circ} \\ I_R - I_L \end{bmatrix}. \tag{3.20}$$

These parameters are measurable quantities, where s_1 is a measure of total intensity, s_2 is the difference between the intensities of linear x- and y- polarised light. s_3 is the difference between linear polarised light of $+45^\circ$and -45°relatively to the x-axis, while s_4 determine the difference between right handed and left handed intensity for circular polarised light.

Degree of polarisation

In the "Handbook of Ellipsometry"[33] the degree of polarisation is defined as the length of the Stokes intensities s_2, s_3 and s_4 divided on the total irradiance(s_1):

$$Degree\ of\ polarisation = \frac{\sqrt{s_2^2 + s_3^2 + s_4^2}}{s_1}. \tag{3.21}$$

If equation (3.21) is zero, the light is unpolarised, while if equation (3.21) is equal one, the wave is totally polarised.

3.3.3 Mueller matrix

The advantages with the Mueller matrix, rather than the Jones matrix, is the ability to determine the state of polarisation of a scattered beam for an arbitrary incident wave, which do not need to be fully polarised. Since light not necessary has to be polarised, but can be for example partially polarised, random polarised or incoherent, such type of light must be treated with the Mueller matrix. By taking a linear transformation of the Stokes vectors for an incoming and outgoing wave it is possible to define a 4×4 Mueller matrix:

$$S_{out} = \mathbf{M} \cdot S_{in}, \tag{3.22}$$

where $\mathbf{M}$ is the Mueller matrix, often normalised to the first element M_{11}. This will also be the case for this thesis, where all the plots of the Mueller matrix are displayed for normalised values of M_{11}.

$$\mathbf{M} = \begin{bmatrix} M_{11} & M_{12} & M_{13} & M_{14} \\ M_{21} & M_{22} & M_{23} & M_{24} \\ M_{31} & M_{32} & M_{33} & M_{34} \\ M_{41} & M_{42} & M_{43} & M_{44} \end{bmatrix} \tag{3.23}$$

One important fact about the Mueller matrix is the possibility to describe the depolarisation property of the sample. If the Mueller matrix is non-depolarised it is called a Mueller-Jones matrix. A relation between the Jones matrix and the Mueller matrix can be derived from the direct product of J and its conjugate J^*:

$$\mathbf{M} = \mathbf{A}(\mathbf{J} \otimes \mathbf{J}^*)\mathbf{A}^{-\mathbf{1}}, \tag{3.24}$$

where $\otimes$ is the Kronecker tensor product and $\mathbf{A}$ is a vector for matrix inversion calculation defined in equation (3.25). For further details of the derivation see Fujiwara [34].

$$\mathbf{A} = \begin{bmatrix} 1 & 0 & 0 & 1 \\ 1 & 0 & 0 & -1 \\ 0 & 1 & 1 & 0 \\ 0 & i & -i & 0 \end{bmatrix}. \tag{3.25}$$

Interpretation of the Mueller matrix

It is important to be aware of that the Mueller matrix has some physical restrictions such as for example it can never have gain (in other words the reflected light beam can never be larger than the incident light beam). Over polarisation of the beam is also not possible. A measured Mueller matrix can although be non-physical due to small measurement errors. The first Mueller matrix element M_{11} describes directly the transmittance and reflectance from the wave.

The Mueller matrix, among others, tells something about depolarisation, which Gil and Bernabeu [35] define as:

$$P_d = \sqrt{\frac{\sum_{i,j} M_{ij}^2 - M_{11}^2}{3M_{11}^2}}. \tag{3.26}$$

If equation (3.26) is equal one it means we achieve non-depolarising, while if $P_d = 0$ is equivalent to completely depolarised light. Depolarisation may occur due to sample properties like: nonuniform film thickness, transparent substrate, sample roughness or instrument properties such as spread in angular frequency of incident light, finite bandwidth of incident light and depolarisation from spectrograph. Another definition of the depolarisation is defined by Chipman [36], where it is defined from the average degree of polarisation.

The Mueller matrix can also measure the degree of anisotropy in the medium. For an isotropic material the Mueller matrix is simple and looks like equation (3.27), where $N = \cos(2\Psi)$, $S = \sin(2\Psi)\sin(\Delta)$ and $C = \sin(2\Psi)\cos(\Delta)$. N, S and C are constrained to the relation: $N^2 + S^2 + C^2 = 1$, and can be used to measure the intensity. The Mueller matrix elements M_{12}, M_{33} and M_{34} define the standard ellipsometry parameters.

$$\mathbf{M_{isotropic}} = \begin{bmatrix} 1 & -N & 0 & 0 \\ -N & 1 & 0 & 0 \\ 0 & 0 & C & S \\ 0 & 0 & -S & C \end{bmatrix}. \tag{3.27}$$

If the sample under investigation have an anisotropic approach, the Mueller matrix becomes slightly more complex, shown in equation (3.28). The definition of the different constants can be fined in the "Handbook of Ellipsometry", page 244 [33]. Still we have a constrained relation for the parameters: $N^2 + S^2 + C^2 + S_{ps}^2 + C_{ps}^2 + S_{sp}^2 + C_{sp}^2 = 1$.

$$\mathbf{M_{anisotropic}} = \begin{bmatrix} 1 & -N - \alpha_{ps} & C_{sp} + \zeta_1 & S_{sp} + \zeta_2 \\ -N - \alpha_{sp} & 1 - \alpha_{sp} - \alpha_{ps} & -C_{sp} + \zeta_1 & -S_{sp} + \zeta_2 \\ C_{ps} + \xi_1 & -C_{ps} + \xi_1 & C + \beta_1 & S + \beta_2 \\ -S_{ps} + \xi_2 & S_{ps} + \xi_2 & -S + \beta_2 & C - \beta_1 \end{bmatrix}. \tag{3.28}$$

The larger differences between the values of $M_{isotropic}$, equation (3.27), and $M_{anisotropic}$, equation (3.28), the more anisotropic is the measured sample.

3.4 Ellipsometry

Ellipsometry is a polarimetric measurement technique, which determine changes in the polarisation state between an incident light beam and the specular reflectance from a sample under investigation. The two parameter that are measured is Δ and Ψ, which are related to Fresnel's amplitude reflection equation:

$$\frac{r_p}{r_s} = \tan(\Psi)e^{i\Delta}, \tag{3.29}$$

where r_p is the p-polarised reflection and r_s is the s-polarised. The reflected intensity recorded in the detector would have the form:

$$I = I_0(1 + \alpha\cos 2A + \beta\sin 2A), \tag{3.30}$$

where the ellipsometric parameters Ψ and Δ can be found taking the Fourier transform of the recorded intensity:

$$\begin{aligned} \Psi &= \arctan\left(\tfrac{1+\alpha}{1-\alpha}\right), \\ \Delta &= \arccos\left(\pm\tfrac{\beta}{\sqrt{1-\alpha^2}}\right). \end{aligned} \tag{3.31}$$

Ellipsometry is a polarimetric measurement technique, useful for characterize dielectric properties of small structures, mainly used for thin films, but can also characterize nanowires. Ellipsometry measure the change in polarisation between an incident wave hitting the substrate and a scattered wave, reflected from the substrate. This reflected wave is also known as specular reflectance.

An ellipsometer consists mainly of four parts: A light source, a polarisation state generator (PSG), a polarisation state analyser (PSA) and a detector [19]. The sketch in Figure 3.4 show a setup of the components in the ellipsometer. $theta_i$ is the incident angle to the illuminated light source and *phi* correspond to the azimuthal rotation of the sample under investigation. Both PSG and PSA consist of at least a linear polariser and a phase retarder, but can also consist of many more optical components depending on the complexity and quality to the ellipsometer.

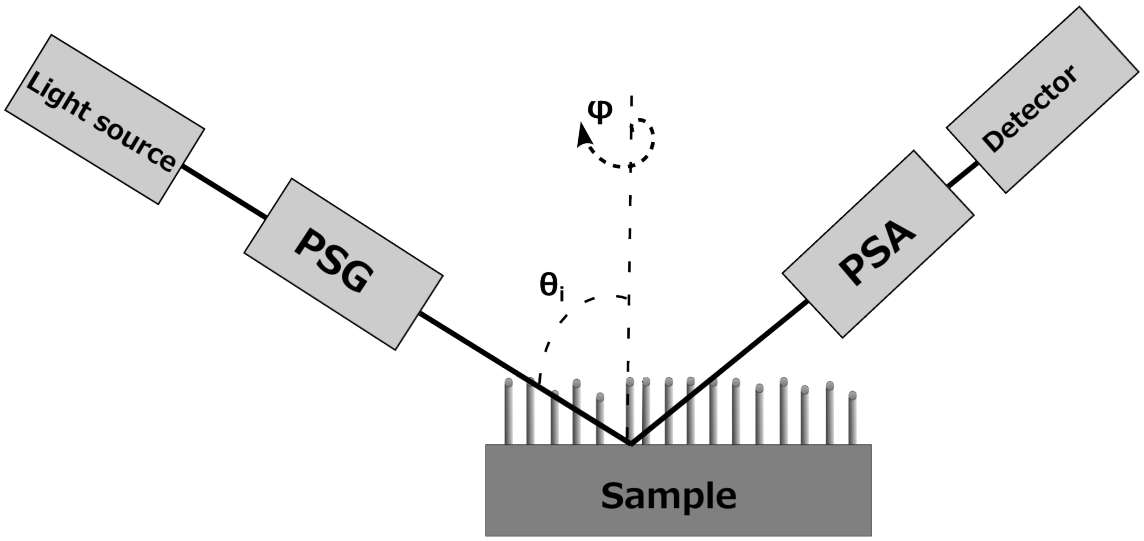

Figure 3.4: A sketch of a set up of an ellipsometer measuring specular reflectance on a nanowires substrate at incident angle θ_i and azimuthal rotation angle ϕ.

The ellipsometry angle Δ measure the phase difference between p-polarised and s-polarised reflected light, while $\tan(\Psi)$ measure the magnitude ratio of the modulus of the amplitude reflection ratio. By only measuring these two parameters it is possible to measure or characterize among others: Film thickness, refractive index, surface roughness, crystallography, interfacial (double layer) region, uniformity and anisotropy. Especially it is a very powerful tool for measuring the refractive index of the sample, since the refractive index depends on the light polarisation to the reflected material. Physical laws such as the law of interference helps to calculate the film thickness and dielectric properties very precisely.

Advantages with ellipsometry in comparison with other optical characterisation techniques, like TEM or SEM, is that it is non-destructive and non-invasive. Other advantages are high accuracy and reproducibility of the measurements, it is very sensitive for nanoscale-structure, and not very susceptible from light source fluctuations. There is also not necessary to have any kind of a reference sample. Losurdo et al. [3] discuss the possibilities for

accurate measurements down to a few nanometers. The main disadvantage is the fact that ellipsometry is a model based technique, where a computer model should be established before the determination of the optical properties. Regression analysis is used to fit the parameters of the raw data iteratively. For some samples, like samples with nanostructures, may this be very complicated.

There are three types of ellipsometries: Standard, generalized and Mueller matrix.

Standard ellipsometry

The standard ellipsometry use Jones transferring matrix and Fresnel's reflection coefficients, r_p and r_s for the different polarisations p and s, to measure the relative difference in amplitude and phase between these reflection coefficients: $\rho = \frac{r_p}{r_s} = \tan(\Psi)e^{i\Delta}$. The Jones matrix for transformation between incident and reflected light are only dependent on Fresnel's equations:

$$J_{standard\ ellipsometry} = \begin{bmatrix} r_p & 0 \\ 0 & r_s \end{bmatrix}. \tag{3.32}$$

Generalized ellipsometry

Since there may exist a coupling between the polarisation states of p- and s-polarised light, the generalized ellipsometry technique was invented. This is the case for anisotropic materials. The generalized Jones matrix is obtained in the same way as for the standard ellipsometry case with generalized ratios, but by measuring 6 angles of Ψ and Δ instead of two.

$$J_{generalized\ ellipsometry} = \begin{bmatrix} r_{pp} & r_{ps} \\ r_{sp} & r_{ss} \end{bmatrix}. \tag{3.33}$$

For isotropic materials there are no coupling between the orthogonal polarization state, which give zero values for the r_{ps} and the r_{sp} coefficients. Then the generalized Jones matrix would be similar to the standard ellipsometry Jones matrix, equation (3.32). The off-block-diagonal elements in the Mueller matrix will then also be zero.

Mueller matrix ellipsometry

If the sample under investigation is smooth and isotropic it is not necessary to measure the spectroscopic Mueller matrix. In fact it is enough to use generalized ellipsometry, but since this is not the case for nanowires, where depolarisation occur, a full spectroscopic Mueller matrix should be considered. The Mueller matrix is obtained from measuring the Stokes parameters. Depending on the material of the sample under investigation an isotropic Mueller matrix(eq. (3.27)) or an anisotropic (eq. (3.28)) Mueller matrix can be recorded.

3.5 Effective medium theory

Imagine we have a layer of heterogeneous material with a surface roughness consisting of many small nanostructures, such as nanowires. If these structures are smaller than the wavelength of light it is possible to approximate this layer as an effective medium layer and estimating a complex effective refractive function for this layer, illustrated in Figure 3.5.

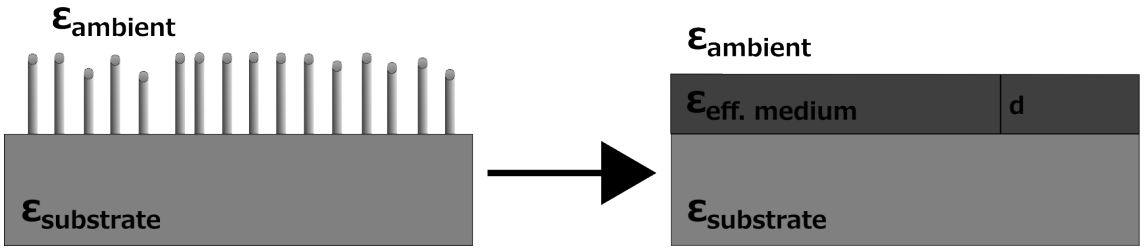

Figure 3.5: A sketch of nanowires on top of a substrate modelled as an effective medium layer, with corresponding effective refractive index $\epsilon_{eff.\ medium}$ and thickness d. $\epsilon_{ambient}$ and $\epsilon_{substrate}$ are the dielectric properties for the surrounding medium and substrate respectively.

For modulating the reflected electromagnetic fields, for an infinite thick substrate a global 4×4 transfer matrix $\mathbf{T}$ is introduced. This transfer matrix describes the total response of the substrate with nanowires.

$$\mathbf{T} = \begin{bmatrix} T_{11} & T_{12} & T_{13} & T_{14} \\ T_{21} & T_{22} & T_{23} & T_{24} \\ T_{31} & T_{32} & T_{33} & T_{34} \\ T_{41} & T_{42} & T_{43} & T_{44} \end{bmatrix}. \tag{3.34}$$

The transfer matrix in equation (3.34) is obtained from the product of all the partial inverted matrices T_{ip} given in equation (3.35). $T_p = e^{ik_0 \Delta d}$ is the partial transfer matrix, which describes the linear translation of the effective medium layer, with corresponding thickness d, derived from the differential equations of first order of Maxwell equations by Berreman [37].

$$T = L_a^{-1}[\prod_{i=1}^{N} T_{ip}(-d_i)]L_f. \tag{3.35}$$

The matrix L_a^{-1} is an incidence matrix describing the ambient medium, defined in Fujiwara (p. 234) [19]:

$$L_a^{-1} = \frac{1}{2} \begin{bmatrix} 0 & 1 & -(n_a \cos\theta_i)^{-1} & 0 \\ 0 & 1 & (n_a \cos\theta_i)^{-1} & 0 \\ (\cos\theta_i)^{-1} & 0 & 0 & \frac{1}{n_a} \\ -(\cos\theta_i)^{-1} & 0 & 0 & \frac{1}{n_a} \end{bmatrix}. \tag{3.36}$$

n_a is the isotropic refractive index to the surrounding medium and θ_i is the incident angle from the illuminated beam. The exit matrix for the substrate L_f is assumed to be

isotropic:

$$L_f = \begin{bmatrix} 0 & 0 & \cos\theta_2 & 0 \\ 1 & 0 & 0 & 0 \\ -n_s\cos\theta_2 & 0 & 0 & 0 \\ 0 & 0 & n_s & 0 \end{bmatrix}, \tag{3.37}$$

where $\cos\theta_2 = \sqrt{1 - (\frac{n_a}{n_s}\sin\theta_i)}$ is calculated from Snell's law, and n_s is the refractive index of the isotropic substrate. The exit matrix is calculated from the total transmitted field within the substrate as a linear combination of eigenvectors. Δ is the characteristic matrix coefficient:

$$\Delta = \begin{bmatrix} -k_x\frac{\epsilon_{zx}}{\epsilon_{zz}} & -k_x\frac{\epsilon_{zy}}{\epsilon_{zz}} & 0 & 1 - \frac{k_x^2}{\epsilon_{zz}} \\ 0 & 0 & -1 & 0 \\ \epsilon_{yz}\frac{\epsilon_{zx}}{\epsilon_{zz}} - \epsilon_{yx} & k_x^2 + \epsilon_{yz}\frac{\epsilon_{zy}}{\epsilon_{zz}} - \epsilon_{yy} & 0 & k_x\frac{\epsilon_{yz}}{\epsilon_{zz}} \\ \epsilon_{xx} - \epsilon_{xz}\frac{\epsilon_{zx}}{\epsilon_{zz}} & \epsilon_{xy} - \epsilon_{xz}\frac{\epsilon_{zy}}{\epsilon_{zz}} & 0 & -k_x\frac{\epsilon_{xz}}{\epsilon_{zz}} \end{bmatrix}. \tag{3.38}$$

The dielectric components are defined for a cartesian coordinate system given in equation (3.9). k_x is the x-component of the incident wave vector: $k_x = n_a\sin\theta_i$. The complex reflection coefficients, equation (3.39) are obtained from the transfer matrix, equation (3.34), a full derivation is shown in Schubert [38].

$$\begin{aligned} r_{pp} &= \tfrac{T_{11}T_{43} - T_{41}T_{13}}{T_{11}T_{33} - T_{13}T_{31}}, \\ r_{ps} &= \tfrac{T_{41}T_{33} - T_{43}T_{31}}{T_{11}T_{33} - T_{13}T_{31}}, \\ r_{ss} &= \tfrac{T_{21}T_{33} - T_{23}T_{31}}{T_{11}T_{33} - T_{13}T_{31}}, \\ r_{sp} &= \tfrac{T_{11}T_{23} - T_{21}T_{13}}{T_{11}T_{33} - T_{13}T_{31}}. \end{aligned} \tag{3.39}$$

The complex reflection coefficients, in equation (3.39) returns the generalized Jones matrix for the transfer matrix:

$$\mathbf{J} = \begin{bmatrix} r_{pp} & r_{ps} \\ r_{sp} & r_{ss} \end{bmatrix}. \tag{3.40}$$

The Jones matrix can be transformed into the Mueller matrix by using equation (3.24).

3.6 Photonic crystal

Photonic crystals are periodic nanostructures, like nanowires, attached like periodic crystal lattices, with alternating refractive index. The photons are affected by the nanostructures and their dielectric material, in such case that for some frequencies there will be absolutely zero transmission. This is called the photonic band gap. If defects are introduced in the crystal, it is possible to control and manipulate the spontaneous emission for an incoming propagation wave, in such case that optical devices can be constructed. Photonic crystals can be classified into one, two or three dimensions depending on the periodicity for the alternating material [39].

An ensemble of positioned nanowires can be regarded as a two dimensional photonic crystal, since they are periodic in two dimensions and homogeneous in the last direction. The

alternating dielectric constants consist here of air and the refractive index of the nanowires. Still are commercial application based on two dimension photonic crystals limited, but one can imagine potential use in a wide range of application such as polariser, fiber, light emitting diodes, etc [39].

3.7 Extinction, Scattering and Absorption

When an electromagnetic light wave propagate into an arbitrary particle, an interaction occur between this particle and the light wave. The light wave can undergo three different types of interaction: Extinction, scattering or absorption. The amount of light which undergoes the different kind of processes depends on the particle size, shape, refractive index, etc.

3.7.1 Extinction

Extinction is characterised as the difference between the intensity of the incoming incident light and the intensity for the continuing propagating wave in same direction after interaction with the particle. Usually would the outgoing wave experience loss of intensity, but can also experience a gain for some materials. Due to conservation of energy extinction gives a relation between the amount of absorbed and scattered light:

$$Extinction = Absorption + Scattering. \tag{3.41}$$

3.7.2 Scattering

Light is said to be scattered if the incident light wave propagating into an obstacle is redistributed in all other directions than the propagating direction. Scattering occur due to differences in the refractive index in the material and the surrounding medium. Depending on the properties of the obstacle we can define different types of scattering: Elastic scattering occur when the wavelength of the illuminated light is the same as the scattered, and the energy is conserved. Mie theory and Rayleigh theory are based on elastic scattering. Inelastic scattering is scattering where the radiated light have an other wavelength than the incoming, such as in fluorescence. Quai-elastic scattering is shift in wavelength of scattered field due to change in position for the object, like in Doppler effect.

Not only does scattering types depend in change of wavelength but can also defined by the photons behaviour: Multiple scattering occur when light hit the obstacle, scatterers, before it hits for example the boundary of the obstacle and undergoes a new scattering process, where light return backwards to the first scattered field and undergoes a subsequent scattering. The photon could in this case also undergo an absorption. For the simulations of the nanowires, we assume only single scattering, where photons move into an obstacle and scatter one single time. This is a good assumption for strong absorbing or low density medias, since there exist a high probability for photon excitation in such medias. Another assumption is that we look at incoherent scattering, where the scattering fields are separated into random directions.

Depending on the ratio between the particle and the wavelength it is possible to approximate incoherent scattering into three different types of elastic scattering approximations: Mie-theory, Rayleigh theory and Rayleigh-Gans-Debye theory. Since the nanowires have approximately the same size as the wavelength of light, this thesis will mainly focus on the Mie theory.

Mie Scattering

Mie theory describes interaction of a plane wave incident on a particle for particles with approximately same size as the wavelength, in case of this thesis wavelength of visible light. These particles primary should be circular or cylindrical, since the solutions of the radiated field, and the angular field, should be separable. Mie scattering explains optical phenomenas such as rainbows, due to refraction between sun light and water molecules. For the software simulations of the nanowires, which are approximated as cylinders, Mie theory is used for calculating the scattered electromagnetic fields.

The electric fields for both the incident wave ($\mathbf{E_i}$) and the outgoing scattered wave ($\mathbf{E_s}$) can be split up into a parallel and a perpendicular field component. A linear transformation between these two electric fields define a 2×2 scattering matrix $\mathbf{S}$:

$$\begin{pmatrix} E_{\parallel s} \\ E_{\perp s} \end{pmatrix} \propto \begin{pmatrix} S_2 & S_3 \\ S_4 & S_1 \end{pmatrix} \begin{pmatrix} E_{\parallel i} \\ E_{\perp i} \end{pmatrix}. \tag{3.42}$$

The components in the scattering matrix $\mathbf{S}$ are dependent on the scattering angle θ and azimuthal angle ϕ for cylindrical geometries. By applying the time average Poynting vector from equation (3.8) for any arbitrary points surrounding the particle, $\mathbf{S}$ can be written as a superposition of Poynting vectors between the incident beam S_i, the scattered wave S_s and the extinct interaction between the incident and scattered wave S_{ext}.

$$\mathbf{S} = S_i + S_s + S_{ext} \tag{3.43}$$

Rayleigh scattering

Rayleigh scattering is an approximation of the Mie theory for scattering of light beams many times smaller than the wavelength. For example do Rayleigh theory describe the reason for why the sky is blue, due to light scattering between the light from the sun and the small air molecules in air.

3.7.3 Absorption

Absorption occur when an incident beam with electromagnetic energy hit an obstacle and undergo a transformation into other energies, like for example thermal energy. Absorption can be detected by measuring the difference between the incoming electromagnetic wave energy and the outgoing wave energy after interaction with the particle. Only materials with a complex refractive index, corresponding to the specific wavelength can undergo an absorption process.

3.8 Calculation of the electromagnetic fields for nanowires

The following section provides the mathematical calculations for the electromagnetic fields when the incident wave undergoes an interaction with one nanowire, approximated as a cylinder. The characteristic hexagonal shape of the nanowires, and the droplet on top, are disregarded in the calculations. We also assume single scattering and disregard both multiple and back scattering.

3.8.1 Single core nanowire

For calculations of the electromagnetic fields for a single homogeneous nanowire we look at one infinite long cylinder an use Mie theory to obtain the scattering series. We assume a monochromatic electromagnetic wave propagating into the cylinder at oblique incidence. The calculation of the extinct and scattered fields can be solved from Maxwell's equations for cylinder coordinates. The solution is based on expansion of the electric and magnetic field components, of the incident and scattered light, into infinite series of cylindrical vector harmonics. By applying boundary conditions at the interface between the different mediums a relation between the electromagnetic fields are obtained. The complete derivation can be found in Bohren and Huffman [30].

Figure 3.6 define θ_i as the angle between the cylinder axis and the incident wave vector (E_i, H_i). ϕ is defined as the azimuthal angle between the x-axis, in the coordinate system, and the projection of the incident wave vector into the plane perpendicular to cylinder axis. Due to the cylindrical symmetry, the scattering fields (E_s, H_S) are independent of the azimuthal angle.

When the incident light wave propagate into an infinite long cylinder the incident electromagnetic fields are dependent of the polarisation of the wave. For example the electric field can either be parallel to the xz-plane (p-polarised light) or perpendicular (s-polarised light).

3.8.2 Calculation of incident electric field parallel to xz-plane

The incident electric field E_i can be expand into the orthogonal vector harmonics M_n and N_n:

$$\mathbf{E_i} = \sum_{n=-\infty}^{\infty} [A_n \mathbf{M_n^{(1)}} + B_n \mathbf{N_n^{(1)}}], \tag{3.44}$$

where A_n and B_n are constants, which are determined by using the orthogonality principles for the vector harmonics and the cylindrical Bessel functions. The solution of the constants are calculated to be $A_n = 0$ and $B_n = \frac{E_0(-i)^n}{k \sin\theta_i}$. The incident electric field consist therefore only of one vector harmonic component: $\mathbf{E_i} = \sum_{n=-\infty}^{\infty} E_n \mathbf{N_n^{(1)}}$. The Maxwell equations for plane harmonic waves, equation (3.5), gives an relation between the electric and the magnetic field components: $\mathbf{H_i} = \frac{-ik}{\omega\mu} \sum_{n=-\infty}^{\infty} E_n \mathbf{M_n^{(1)}}$, where $E_n = \frac{E_0(-i)^n}{k \sin\theta_i}$.

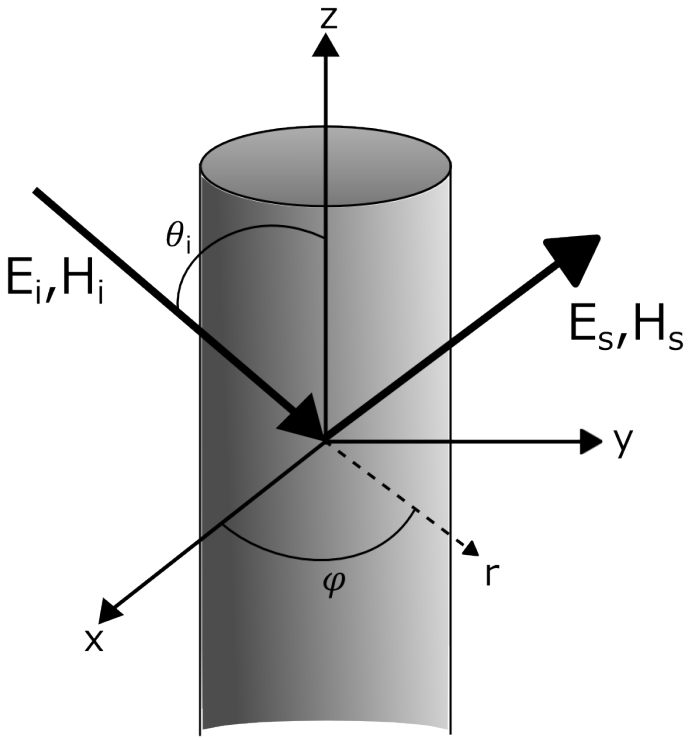

Figure 3.6: A sketch of the defined coordinate systems for an oblique incident wave (E_i, H_i) on a single cylinder for both cartesian and cylinder coordinates. The scattering fields are noted E_s, H_s.

On a similarly way it is possible to calculate the scattered fields for the electromagnetic waves:

$$\begin{aligned} \mathbf{E_s} &= -\sum_{n=-\infty}^{\infty} E_n[b_{n1}\mathbf{N_n^{(3)}} + ia_{n1}\mathbf{M_n^{(3)}}], \\ \mathbf{H_s} &= \tfrac{ik}{\omega\mu}\sum_{n=-\infty}^{\infty} E_n[b_{n1}\mathbf{M_n^{(3)}} + ia_{n1}\mathbf{N_n^{(3)}}]. \end{aligned} \tag{3.45}$$

By applying boundary conditions given in equation (3.7), it is possible to calculate expressions for the scattering coefficients a_{n1} and b_{n1}, given in equation (3.46) and (3.47).

$$a_{n1} = \frac{C_n V_n - B_n D_n}{W_n V_n + iD_n^2}. \tag{3.46}$$

$$b_{n1} = \frac{W_n B_n - iD_n C_n}{W_n V_n + iD_n^2}. \tag{3.47}$$

The constants B_n, C_n, D_n, V_n and W_n are defined as following:

$$\begin{aligned}
B_n &= \zeta[m^2\zeta J_n'(\eta)J_n(\zeta) - \eta J_n(\eta)J_n'(\zeta)],\\
C_n &= n\cos\theta_i\eta J_n(\eta)J_n(\zeta)(\tfrac{\zeta^2}{\eta^2}-1),\\
D_n &= n\cos\theta_i\eta J_n(\eta)H_n^{(1)}(\zeta)(\tfrac{\zeta^2}{\eta^2}-1),\\
V_n &= \zeta[m^2\zeta J_n'(\eta)H_n^{(1)}(\zeta) - \eta J_n(\eta)H_n^{'(1)}(\zeta)],\\
W_n &= i\zeta[\eta J_n(\eta)H_n^{'(1)}(\zeta) - \zeta J_n'(\eta)H_n^{(1)}(\zeta)],
\end{aligned} \tag{3.48}$$

where $\zeta = x\sin\theta_i$, $\eta = x\sqrt{m^2-\cos^2\theta_i}$ and $x = ka$. The magnetic permeability is approximated to be the same in the cylinder and the surrounding medium, and therefore disappear from equation (3.48). J_n and J_n' are the Bessel function and its derivative, while $H_n^{(1)}$ and $H_n^{'(1)}$ are the Hankel function of first kind and its derivative. a is the radius of the cylinder, while m is the ratio between the refractive index of the material and the ambient medium.

3.8.3 Calculation of incident electric field perpendicular to xz-plane

For a s-polarised incident wave the electric field can be expand into vector harmonics consisting of only M_n:

$$\mathbf{E_i} = -i\sum_{n=-\infty}^{\infty} E_n\mathbf{M_n^{(1)}}. \tag{3.49}$$

By using the same argumentation as for section 3.8.2, the scattered electric field can be written as:

$$\mathbf{E_s} = \sum_{n=-\infty}^{\infty} E_n[ia_{n2}\mathbf{M_n^{(3)}} + b_{n2}\mathbf{N_n^{(3)}}]. \tag{3.50}$$

By again applying boundary conditions for the interface between the two mediums, equation (3.7), the scattering coefficients a_{n2} and b_{n2} can be solved:

$$a_{n2} = -\frac{A_nV_n - iC_nD_n}{W_nV_n + iD_n^2}, \tag{3.51}$$

$$b_{n2} = -i\frac{C_nW_n + iA_nD_n}{W_nV_n + iD_n^2}. \tag{3.52}$$

The constants B_n, C_n, D_n, V_n and W_n are similarly defined as in equation (3.48), while the constant A_n is defined in equation (3.53). The variables ζ and η is also defined the same as previous.

$$A_n = -i\zeta[\zeta J_n'(\eta)J_n(\zeta) - \eta J_n(\eta)J_n'(\zeta)]. \tag{3.53}$$

3.8.4 The scattering matrix for an infinite long cylinder

The scattering coefficients can be expanded into infinite series:

$$
\begin{aligned}
S_1 &= b_{01} + 2\sum_{n=1}^{\infty} b_{n1}\cos(n\Phi), \\
S_2 &= a_{02} + 2\sum_{n=1}^{\infty} a_{n2}\cos(n\Phi), \\
S_3 &= -2i\sum_{n=1}^{\infty} a_{n1}\sin(n\Phi), \\
S_4 &= -2i\sum_{n=1}^{\infty} b_{n2}\sin(n\Phi) = -S_3,
\end{aligned}
\tag{3.54}
$$

where S_1, S_2, S_3 and S_4 correspond to the different components in the scattering matrix defined in equation (3.42). n is the order of the cylindrical vector harmonics and Φ is the outgoing specular angle, indicating a phaseshift between the incoming and outgoing wave: $\Phi = \pi - \phi$. The scattering coefficients relates to the amplitudes of the incident and scattered electromagnetic fields. For example a_{11} is proportional to the electromagnetic field, while a_{21} is quadrupolar and so on.

3.8.5 Calculation of scattering coefficients for a core-shell nanowire

Nanowires are not necessarily grown of a single material, but may be radially grown consisting of two different materials for among other increasing the yield. This core-shell structure will change the optical properties of the electromagnetic fields due to differences in refractive index between the two mediums.

The solutions for the scattering coefficients are based on the same calculation principles as for a single nanowire with expanding of cylindrical vector harmonics for p- and s-polarised light, but the solution become more complex due to an extra interface for the propagating wave. We look at an infinite long concentric cylinder, with oblique incidence, with same coordinate systems as in Figure 3.6, but with an extra shell. Instead of calculating the scattering coefficients from the cylindrical vector harmonics, are the numerical simulation based on the calculations from Gurwich et al. [40]. This solution of the scattering fields are based on a recursive algorithm for infinite layers of a concentric cylinders. The scattered field for p-polarised light is given to be [40]:

$$
a_{n1} = T_n(\xi)\frac{\xi^2 L_5 L_2 - g_j n^2 \cos^2\zeta (v_j^2-1)^2}{\xi^2 L_2 L_3 - g_j n^2 \cos^2\zeta (v_j^2-1)^2},
\tag{3.55}
$$

$$
b_{n1} = -i\frac{g_j (v_j^2-1)\xi n \cos\zeta T_n(\xi) L_1}{\xi^2 L_2 L_3 - g_j n^2 \cos^2\zeta (v_j^2-1)^2},
\tag{3.56}
$$

while the scattered field for s-polarised light are:

$$
a_{n2} = i\frac{g_j (v_j^2-1)\xi n \cos\zeta T_n(\xi) L_1}{\xi^2 L_2 L_3 - g_j n^2 \cos^2\zeta (v_j^2-1)^2},
\tag{3.57}
$$

$$
b_{n2} = T_n(\xi)\frac{\xi^2 L_4 L_3 - g_j n^2 \cos^2\zeta (v_j^2-1)^2}{\xi^2 L_2 L_3 - g_j n^2 \cos^2\zeta (v_j^2-1)^2}.
\tag{3.58}
$$

n is the number of layers, in this case n=2. The definition of the rest of the constants and functions can be fined in Gurwich et al. [40]. The validity of this algorithm compared

to the exact physical calculations of the Mie theory are also discussed in the paper, and seems to fit good with experimental theory.

3.8.6 Efficiencies and cross section

Cross section is a measure of light intensity, removed from an incident light beam, by a unit area. The cross section gives an indication about how large a non-resonant particle in the light path must be, before it blocks a fraction of the incident light intensity. The cross section is derived from the ratio between the energy W and irradiance I. Due to conservation of energy the extinct cross section C_{ext} is the sum of absorbed cross section C_{abs} and C_{sca}:

$$\begin{aligned} C_{ext} &= C_{abs} + C_{sca}, \\ \frac{W_{ext}}{I} &= \frac{W_{abs}}{I} + \frac{W_{sca}}{I}. \end{aligned} \tag{3.59}$$

The efficiency Q describes the fraction of light extinct, scattered or absorbed by the object. Q is expressed as the ratio between the cross section and the geometrical cross section:

$$\begin{aligned} Q_{ext} &= \frac{C_{ext}}{G}, \\ Q_{sca} &= \frac{C_{sca}}{G}, \\ Q_{abs} &= \frac{C_{abs}}{G}, \end{aligned} \tag{3.60}$$

where G is the geometrical cross section area, to the particle, projected onto a plane perpendicular to the incident wave. For example a scattering efficiency equal one, means that the intensity of the incident light, removed due to cylinder scattering is the same as the intensity removed by a non-resonant particle with same dimension as the cylinder. In an infinite cylinder G corresponds to the diameter d of the cylinder per unit length.

Since the cross section of scattering and absorption for an infinite long cylinder is infinite we look at the efficiencies for infinite cylinders per unit length. Cross section and efficiencies depend on the polarisation of the light. The derivation of the efficiencies with polarisation parallel to xz-plane(p-polarised) and perpendicular to the xz-plane(s-polarised) can be found in Bohren and Huffman (p. 204) [30].

$$\begin{aligned} Q_{sca,1} &= \tfrac{2}{x}(|b_{01}|^2 + 2\sum_{n=1}^{\infty}(|b_{n1}|^2 + |a_{n1}|^2)), \\ Q_{ext,1} &= \tfrac{2}{x}Re(|b_{01}|^2 + 2\sum_{n=1}^{\infty} b_{n1}), \\ Q_{sca,2} &= \tfrac{2}{x}(|a_{02}|^2 + 2\sum_{n=1}^{\infty}(|a_{n2}|^2 + |b_{n2}|^2)), \\ Q_{ext,2} &= \tfrac{2}{x}Re(|a_{02}|^2 + 2\sum_{n=1}^{\infty} a_{n2}), \end{aligned} \tag{3.61}$$

where $x = kr$. The cross section can be found from equation (3.60), with G is equal to the diameter($G = 2r$), and the absorption efficiencies can be calculated from the conservation of energy relation, in equation (3.59):

$$\begin{aligned} Q_{abs,1} &= Q_{ext,1} - Q_{sca,1}, \\ Q_{abs,2} &= Q_{ext,2} - Q_{sca,2}. \end{aligned} \tag{3.62}$$

For unpolarised light the efficiencies can be written as an average between the two polarisations: $Q_x = \frac{1}{2}(Q_{x1} + Q_{x2})$. Where x describe the different types of light interaction.

4. Methodology

This thesis can be divided into two individual parts. First a software algorithm was created to simulate scattering and absorption looking at one single nanowire, before effective medium theory was applied to calculate the specular reflectance from a bunch of nanowires on a substrate. This algorithm have further been extended to deal with a core-shell structure for nanowires made of two different materials, a core of GaAs and a shell of AlGaAs. The second part, and also the main part of this thesis is about polarimetric characterization of nanowires. The Mueller matrix is measured in the specular direction with an ellipsometer. The wires under investigation have either been random grown or positioned with a fixed distance in between each other. Mainly GaAs wires have been investigated, but also some core-shell structures, with a shell consisting of AlGaAs or GaAsSb have been under investigation, as well as varying the length of the nanowires.

4.1 Implementation of software algorithm

For simulation of the far field of the Mie scattered electromagnetic wave, some simplifications have been made. First it was assumed that the nanowires have a cylindrical shape, instead of a hexagonal. This is a normal approximation of a nanowire, which also can be viewed clearer in the SEM pictures, Figure 4.7 and Figure 4.6, where it is not easy to see whenever the nanowires have a cylindrical or a hexagonal shape. First at very close distance the characteristic hexagonal shape is detectable. In Figure 4.5 is easier to see the characteristic hexagonal shape. The nanowires are also grown with a droplet on top due to dissolution of Gallium and Arsenide vapor into the solid under the vapor liquid solid growth technique. The droplet can be neglected from the calculations since we assume infinite long nanowires, which is a good approximation for diameters many times shorter than length.

In the calculation of the scattering matrix (eq. (3.54)) and the efficiencies (eq. (3.61)) infinite long sums appear. The program deal with these infinite expressions by stopping the addition when the sum converges for large enough values of n, which happen when the sum of the scattering coefficients $a_{n1} + b_{n1} + a_{n2} + b_{n2}$ are significantly small.

4.1.1 Implementation of a core-shell structure

After assuring that the scattering simulation works for a nanowire solely consisting of one material. The program was further extended to deal with a core-shell structure, where the nanowires consist of two different materials. There are some combinations of core-shell

nanowires which are more attractive than others, such as GaAs and AlGaAs, since they have approximately same lattice constant, which minimize the strain.

The scattering coefficients was first tried implemented by calculating the physical electromagnetic fields for both TE and TM polarisation, similar to the single core nanowire, but for concentric cylinder with one shell. Since this was not done in neither Huffman [30] or Van Hulst [32], it turned out to be difficult to solve correctly. Therefore the scattering field implemented into the software from a recursive algorithm made by Gurwich et al. [40]. This recursive algorithm works for infinity amount of shells. The validity of this algorithm compared to the actual physical calculated electromagnetic fields are further discussed in the same paper, and seem to be reliable. By using the scattering coefficients from Gurwich et al. with two shells, the scattered far fields for a concentric cylinder was added to the software simulations. The expressions for all the scattering components and the derivation can all be found in [40].

4.1.2 Simulation of specular reflectance using effective medium theory

Whenever the nanowires consist of a core-shell structure or not, the implementation of the specular reflectance of an ensemble of nanowires is the same. The only difference will be in the scattering components of the electromagnetic fields, for s and p polarised light, due to differences in refractive index between the core and the shell. The effective medium theory was implemented from Berreman-Schubert formalism, for an ensemble of nanowires lying on top of an semi-infinite thick substrate.

The simulations looks solely at the scattered far field from an incident light beam, which interact on a single nanowire. Even though the distance between the nanowires are small enough such that it should occur some scattering interaction between the wires, we assume the distance is far enough such that multiple scattering is negligible and only single scattering occur. Since the substrate, the nanowires are grown on top of, is substantially thicker than the length of the nanowires, we can assume the substrate to be semi-infinite thick.

The effective refractive indices are calculated from equation (3.12), for both p- and s-polarised light. The p-polarised effective refractive index is calculated from the scattering infinite series S_1, in equation (3.54): $\mathbf{S_p}$=S_1, while the s-polarised effective refractive index is calculated from the scattering infinite series S_2, in equation (3.54): $\mathbf{S_s}$=S_2.

The scattering matrix $\mathbf{S}$ is dependent of incident angle θ_i, the azimuthal incident angle ϕ, scattered angle Θ, scattered azimuthal angle Φ, radius r and wavelength λ. For simplicity we assume a specular relation between the incidence and scattered angles: $\Phi = \pi - \phi$ and $\Theta = \pi - \theta_i$, so the scattering matrix is only dependent of r, θ_i, ϕ and λ.

The amount of particles per unit volume N was estimated after measuring average distances between the nanowires and average length of the nanowires from SEM images. Notice that the nanowires are no longer approximated to be infinite long in the effective medium approximation, but have a finite length d. For making a more precise estimation of the nanowires, grown on top of a substrate. it could be more suitable to estimate N through the volume filling fraction of GaAs nanowires.

The nanowires are assumed to be oriented in z-direction with symmetrical behaviour in x- and y-direction, in the cartesian coordinate-system. It is possible to look at the cylinder as

an anisotropic uniaxial crystal with the permittivity tensor similar to equation (3.11). The tensor will have an extraordinary permittivity axis for ϵ_ζ, and the ordinary permittivity axis for ϵ_ξ and ϵ_η. We divide the incoming beam into a parallel (p-polarised) and a perpendicular (s-polarised) component, and assume that one polarisation propagate in the z-direction, while the other propagate in the x-y-direction. This define a new complex refractive tensor, ϵ_r, for p- and s-polarised light expressed in equation (4.1). ϵ_s corresponds to the dielectric function for s-polarised light and ϵ_p the dielectric function for p-polarised light, calculated from the effective refractive index:

$$\epsilon_r = \begin{pmatrix} \epsilon_s & 0 & 0 \\ 0 & \epsilon_s & 0 \\ 0 & 0 & \epsilon_p \end{pmatrix}. \tag{4.1}$$

The ambient medium is assumed to be vacuum. A total transfer matrix T is calculated from equation (3.35) and describe the total response of all the entire layers of film, where we in this case only look at one layer. The Jones matrix can be calculated from the complex reflection coefficients (eq.(3.39)) and then converted into an isotropic Mueller matrix.

4.2 Ellipsometry measurements

For the optical characterization of the samples a J. A. Woollam Co. ellipsometer was used. The ellipsometer characterize the samples via a variable multichannel dual rotating spectroscopic Mueller matrix ellipsometer (RC2). A collimated light source illuminating 150 W from a Xenon-lamp with spectral range between 210 nm and 1690 nm. The detector system consist of a combination of Si and InGaAs spectrographs. Focus probes with 80 mm focal length, were attached to minimise the beam spot size to approximately 0.3 mm. The measurements were preformed between incidence angles of 30° to 80°, and by change in the azimuthal rotation from 0° through an entire loop of 360° of the incidence plane. The measurements were preformed for an acquisition time of 20 seconds per spectrum. The M_{ij} elements have all been normalised to the total intensity of the first element M_{11}. A picture of the set up can be seen in Figure 4.1.

During the measurements, the ellipsometer camera was used to detect possible scratches and errors on top of the substrate. Measurements on these area was therefore avoided. Figure 4.2 show the illuminated beam spot on sample SC504 for different incidence angles and azimuthal rotations. The location of scratches and defects can clearly be spotted on the morphology of the sample. The matte areas are places where the nanowires were not affected of defects.

Before any sample measurements were done, a straight through measurement on air was used to check the quality of the calibration. An isotropic test wafer of $25nmSiO_2/c-Si$ was also used to check the quality of the calibration, as well as the quality of the alignment.

4.2.1 Sample description

The samples under investigation in this thesis have mainly been GaAs nanowires grown on top of a p-type Si(111) substrate, grown with a Molecular beam epitaxy at 640°C along the

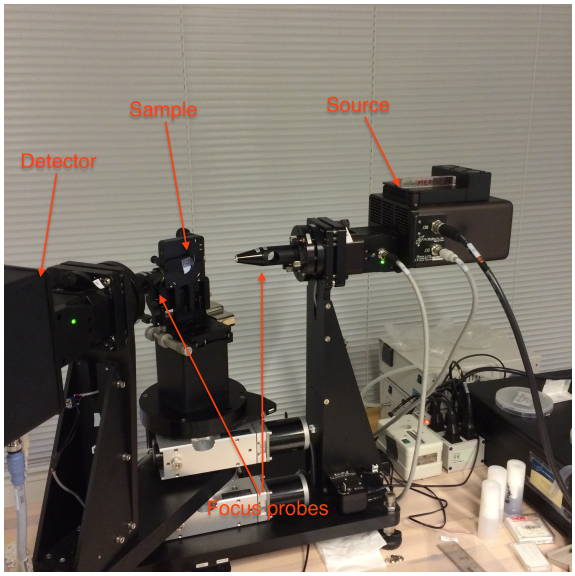

Figure 4.1: The laboratory set up of the ellipsometer with attached focus probes. The incoming light is illuminated from the source in the right part of the picture and the detector is seen on the left side. A sample is mounted on a standard stage i the middle, and investigated for an incident angle of 65°

[111]B direction with homogeneous diameters. The nanowires were either random grown nanowires or positioned oriented. Some nanowires were grown with a core-shell structure consisting of GaAs as core material and a shell of GaAsSb or AlGaAs. Different SEM images of each samples was used to estimate an average length, diameter and distance between the wires. By either calculating the Fourier spectra of top view SEM pictures (seen in Figure 4.3, or measuring length and angles between the nanowires.

For the power spectra in Figure 4.3 it is possible to detect hexagonal symmetry. The stripes indicate disorder in the sample. A perfect hexagonal lattice should have a DC point in the center with dots around, which are difficult to detect from the images.

Table 4.1, summarize a list of SEM measured average values and standard deviation, for different samples, used to measure the specular Mueller matrix ellipsometry in this thesis. We have been looking at nanowires with different length between around 4 μm to under 1 μm. The height was measured from bottom of the nanowires to the bottom of the droplet at the top of the wires, while the distance between the nanowires was measured from the middle of the nanowire to the neighbouring nanowire at different locations of the sample.

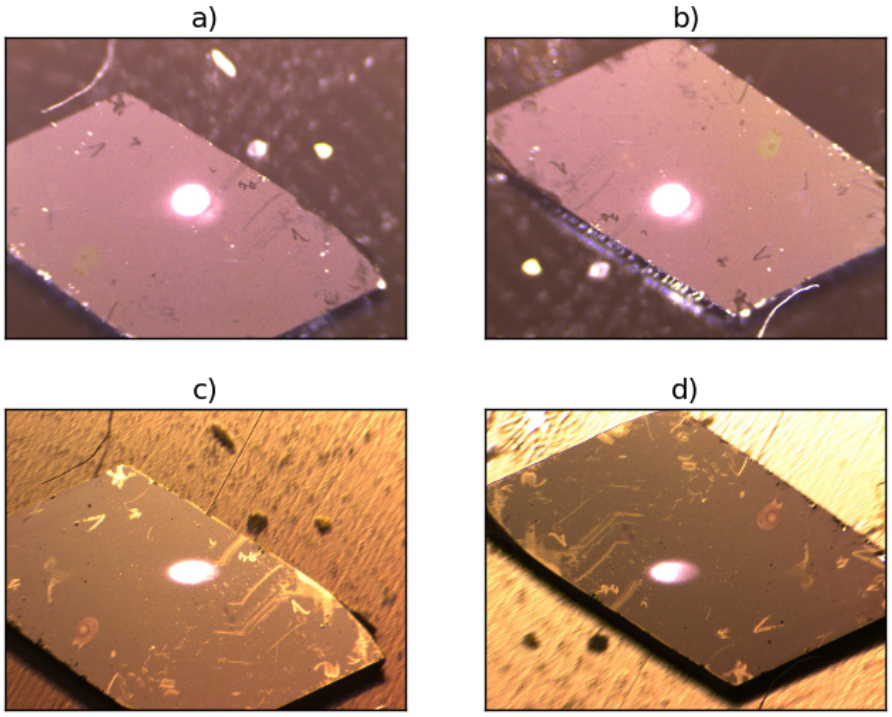

Figure 4.2: A picture of the beam spot on sample SC504 for different Incident angles (θ_i) and azimuthal rotations (ϕ): a) Beam position at $\theta_i = 45°$ and $\phi = 0°$. b) Beam position at $\theta_i = 45°$ and $\phi = 180°$. c) Beam position at $\theta_i = 65°$ and $\phi = 0°$. d) Beam position at $\theta_i = 65°$ and $\phi = 180°$.

Sample	Growth type	Length [μm]	Radius [nm]	Distance [μm]	Material
SC504	Pattern	1.4 ± 0.1	58 ± 5	1.0 ± 0.1	GaAs
SC507	Random	3.8 ± 0.3	52 ± 7	0.6 ± 0.2	GaAs
SC534	Random	0.6 ± 0.2	35 ± 7	0.6 ± 0.1	GaAs
SC538	Pattern	2.3 ± 0.1	69 ± 6	0.9 ± 0.1	GaAs/GaAsSb
SC560	Random	0.7 ± 0.1	32 ± 4	0.3 ± 0.1	GaAs
SC570	Pattern	3.2 ± 0.1	198 ± 13	1.0 ± 0.1	GaAs
SC571	Pattern	3.1 ± 0.2	168 ± 15	1.0 ± 0.1	GaAs/AlGaAs

Table 4.1: An overview over average measured length, radius and distance in between the nanowires, as well as standard deviation. These values was later used in the numerical simulations for emulating the samples as close as possible. The nanowires are either grown random or positioned in a hexagonal pattern. Sample SC538 and SC571 have two materials, which means they are grown in a core-shell structure.

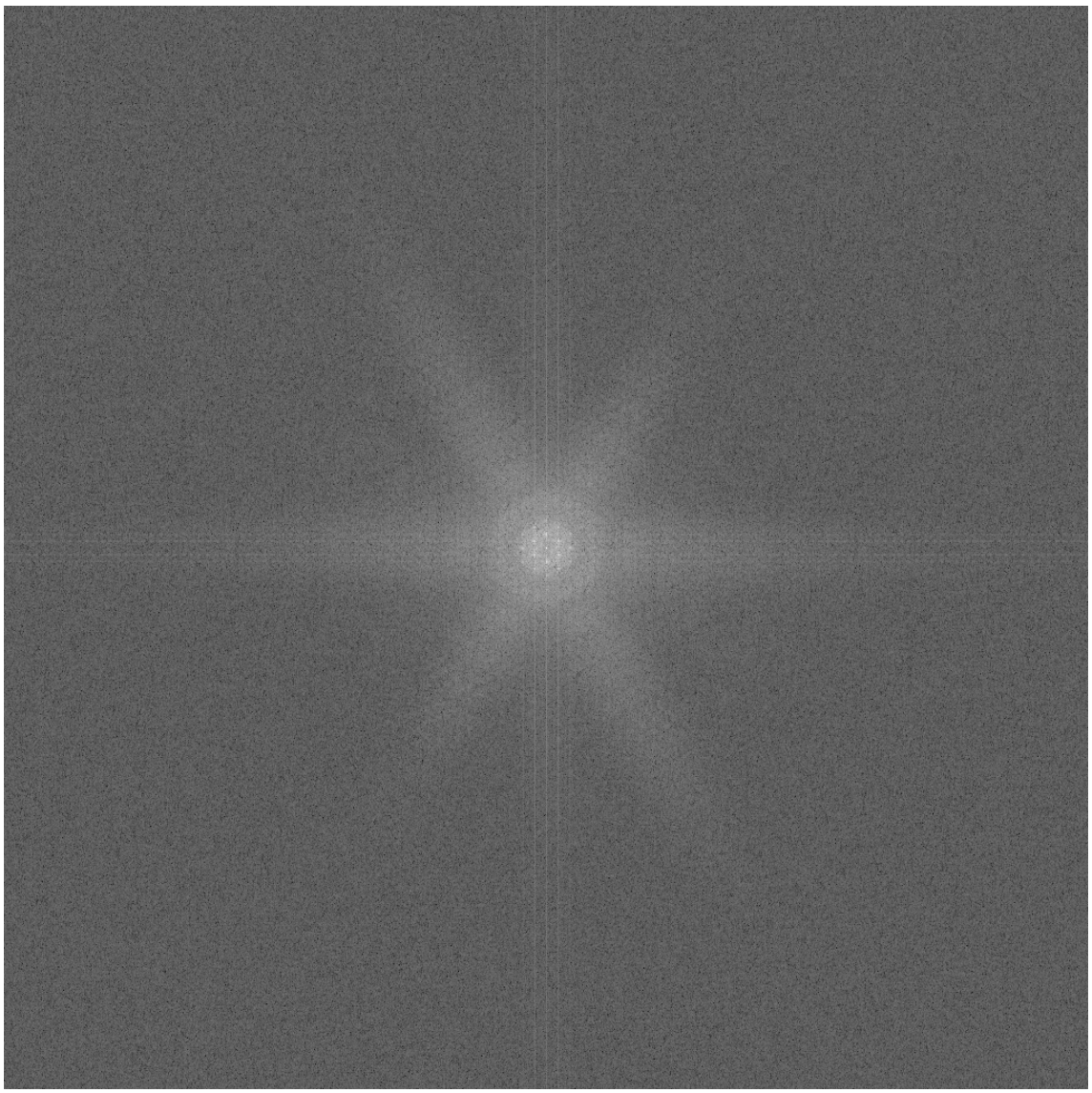

Figure 4.3: The calculated Fourier spectra for a top view SEM image, Figure 4.4 for sample SC571. It is possible to detect the hexagonal symmetry, as well as dots in the center. The stripes indicate some disorder in the lattice.

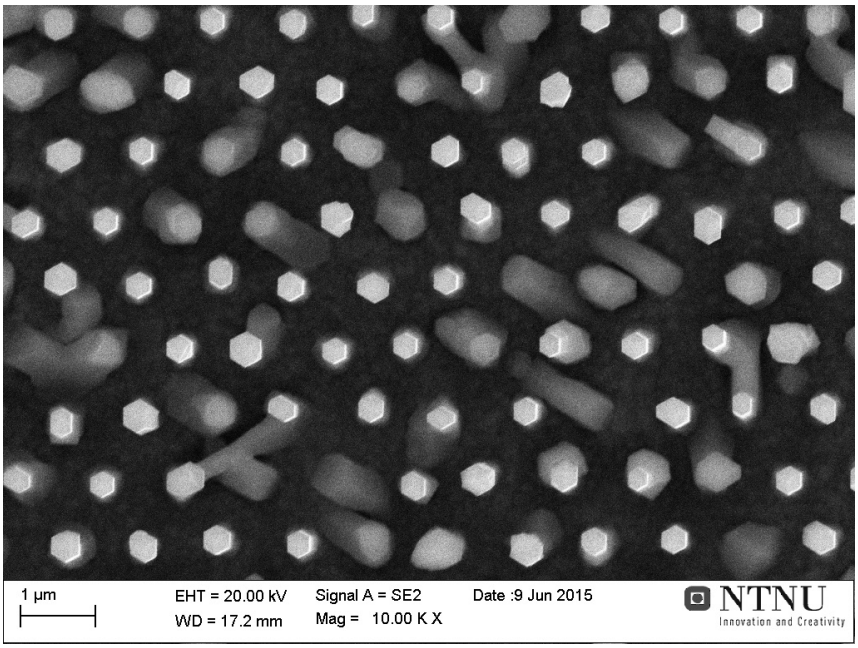

Figure 4.4: A top view SEM image for positioned growth core-shell nanowires, sample SC571.

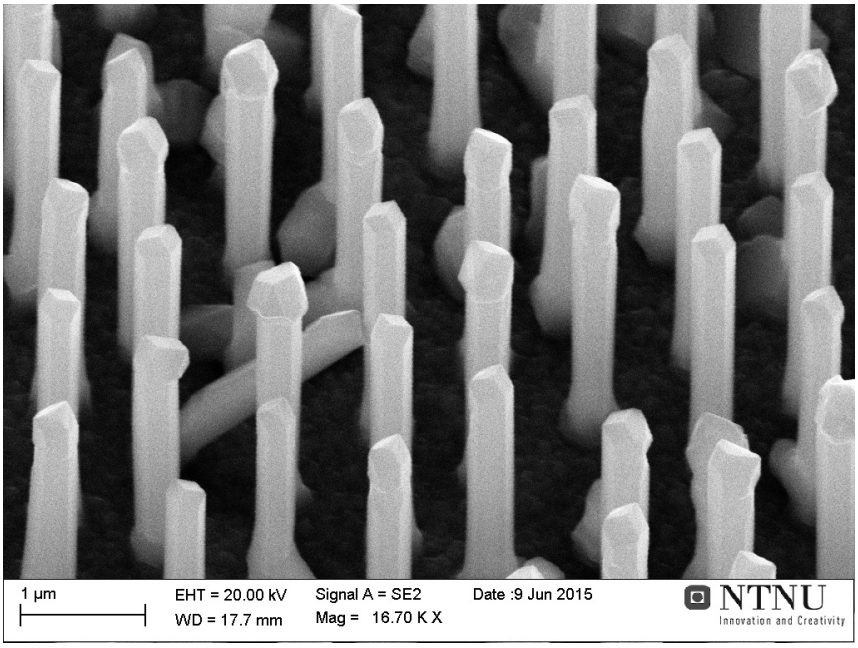

Figure 4.5: A tilted SEM image at 30°from top view for positioned growth core-shell nanowires, sample SC571.

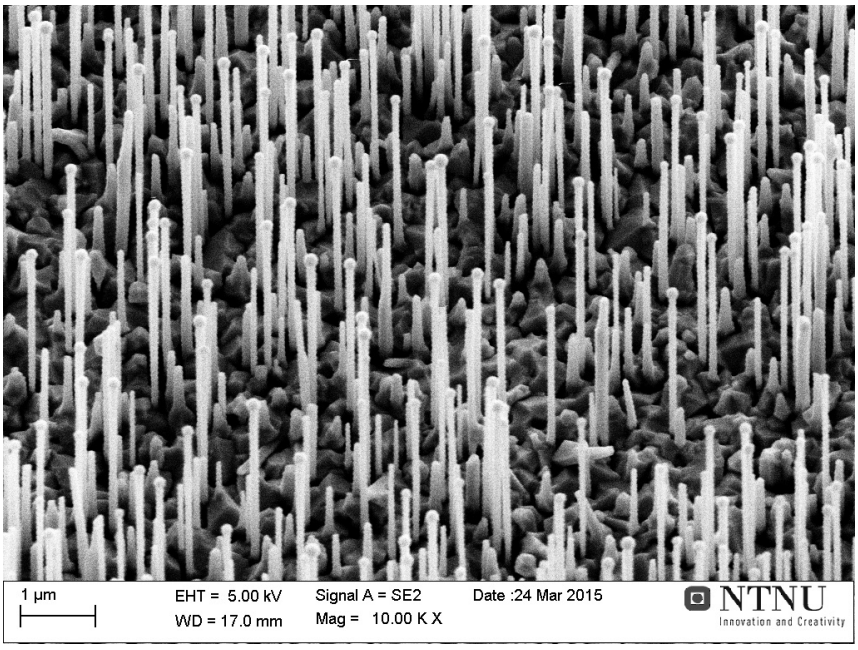

Figure 4.6: A tilted SEM image at 30°from top view for positioned growth nanowires, sample SC507.

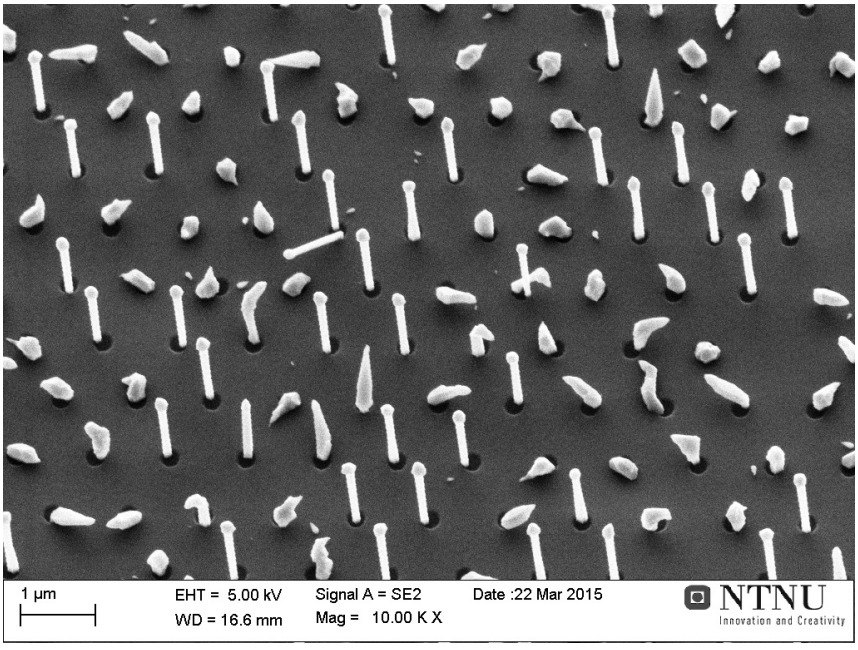

Figure 4.7: A tilted SEM image at 30°from top view for positioned growth nanowires, sample SC504.

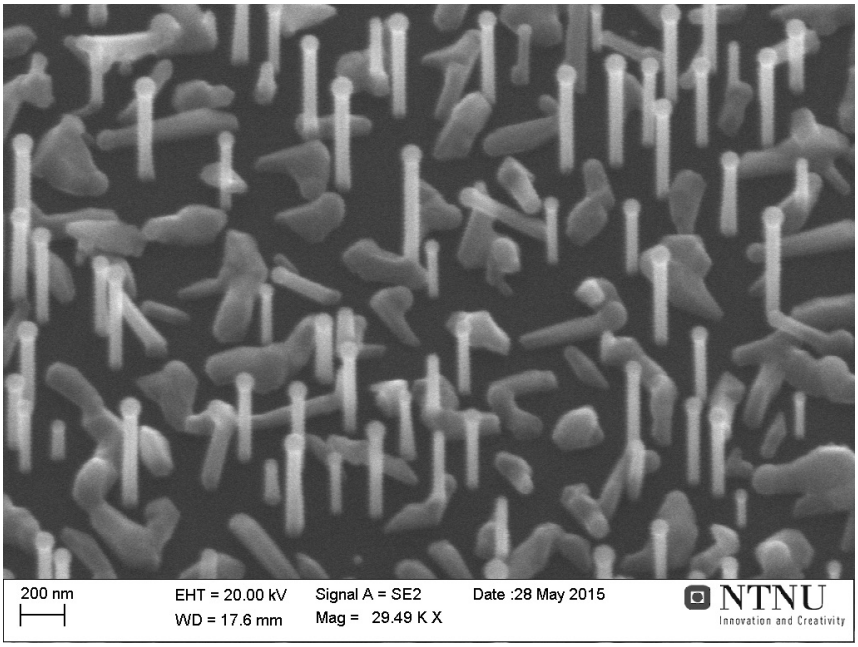

Figure 4.8: A tilted SEM image at 30°from top view for positioned growth nanowires, sample SC560.

5. Results and discussions

This chapter display the results for both numerical simulations and measured spectroscopic Mueller matrix ellipsometry. The simulated and measured Mueller matrix will be compared and discussed, as well as the optical properties of the samples for a complete azimuthal rotation.

5.1 Software simulations

The algorithm can be divided into two parts, first calculating the scattering fields looking at one single nanowire, thereafter include effective medium theories to look at an ensemble of nanowires. Part of the effective medium theory algorithm was created by Post. Doc. Lars Martin Sandvik Aas [41] for his doctoral thesis. All simulations use the full dispersion properties of the complex refractive index for GaAs or Si with vacuum as surrounding medium.

5.1.1 Absorption and scattering for a single nanowire

The cornerstone of the algorithm is to calculate the scattering matrix of the far field to one single cylinder. Before the algorithm could be extended to include effective medium calculations it was import to be sure to have correct calculated scattering fields. Since it was not possible to acquire any measurements of absorption or scattering looking solely at one nanowire, the results have been compared with scientific papers: Grzlea [9] did simulations of absorption and scattering on Indium-phosphide (InP) nanowires. While Cao et al. [7] and Bronstrup et al. [8] did the same for Germanium (Ge) and Silicon (Si) respectively. By changing the refractive index of GaAs, in the algorithm to any of the above mentioned materials, it is possible to reproduce exactly the same results as any of the above mentioned papers. This gave a strong indication of correct calculated scattering fields. The scattering and absorption efficiencies can be plotted by varying either wavelength of light, the nanowire radius or incident angle:

Scattering and absorption efficiencies as function of radius and wavelength

For all the absorption efficiencies in Figure 5.1b), d) and f) it is clearly seen that the nanowires support the Mie resonances. The resonance modes lays tighter for increasing values of the radius. Even though the Mie resonance increases the highest absorption efficiencies are located at small radii, at first resonance mode. There do not exist any absorption over the band gap energy, $E_g = 1.42$ eV for GaAs, where the imaginary part of

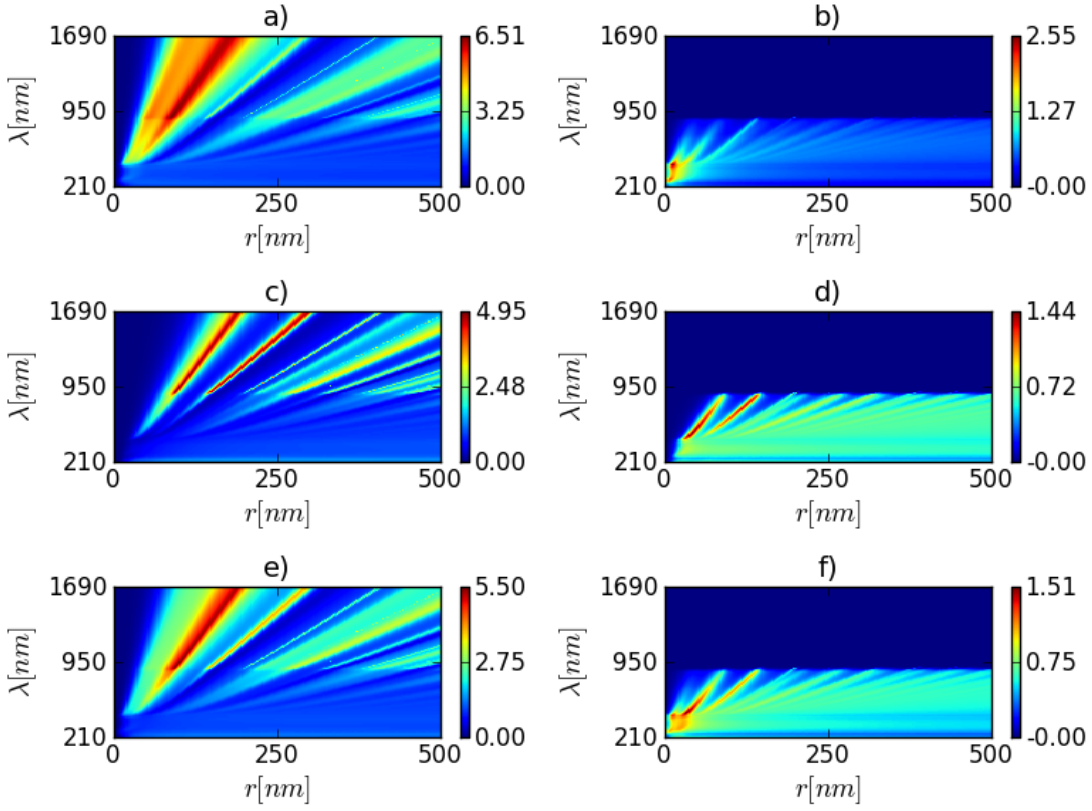

Figure 5.1: Simulated scattering (left part of the figure) and absorption (right part of the figure) efficiencies as function of radius r and wavelength λ. The incident angle θ_i is set to 45°. a) Scattering efficiency for p-polarised light. b) Absorption efficiency for p-polarised light. c) Scattering efficiency for s-polarised light. b) Absorption efficiency for s-polarised light. a) Scattering efficiency for unpolarised light. b) Absorption efficiency for unpolarised light.

the refractive index is zero. This correspond to a wavelength $\lambda = 873$ nm, for longer wavelengths the material is transparent. The same behaviour follows for other semiconductors, like Si, Ge and InP at their specific band gap wavelength.

The scattering efficiencies in Figure 5.1a), c) and e) it is also possible to detect the band gap, where there are a slightly change in color. The scattering efficiencies does not decrease for increasing wavelength over the band gap, since the real component of the refractive index is constant, but also due to zero absorption. The extinction efficiencies will also increase for zero absorption. The resonant modes for the scattering efficiencies lay wider between each other, than for the absorption efficiencies. The resonant modes arise due to the wavelengths in the cross section of the cylinder match their circumference. p-polarised light seems to absorb and scatter more than s-polarised according to the efficiencies.

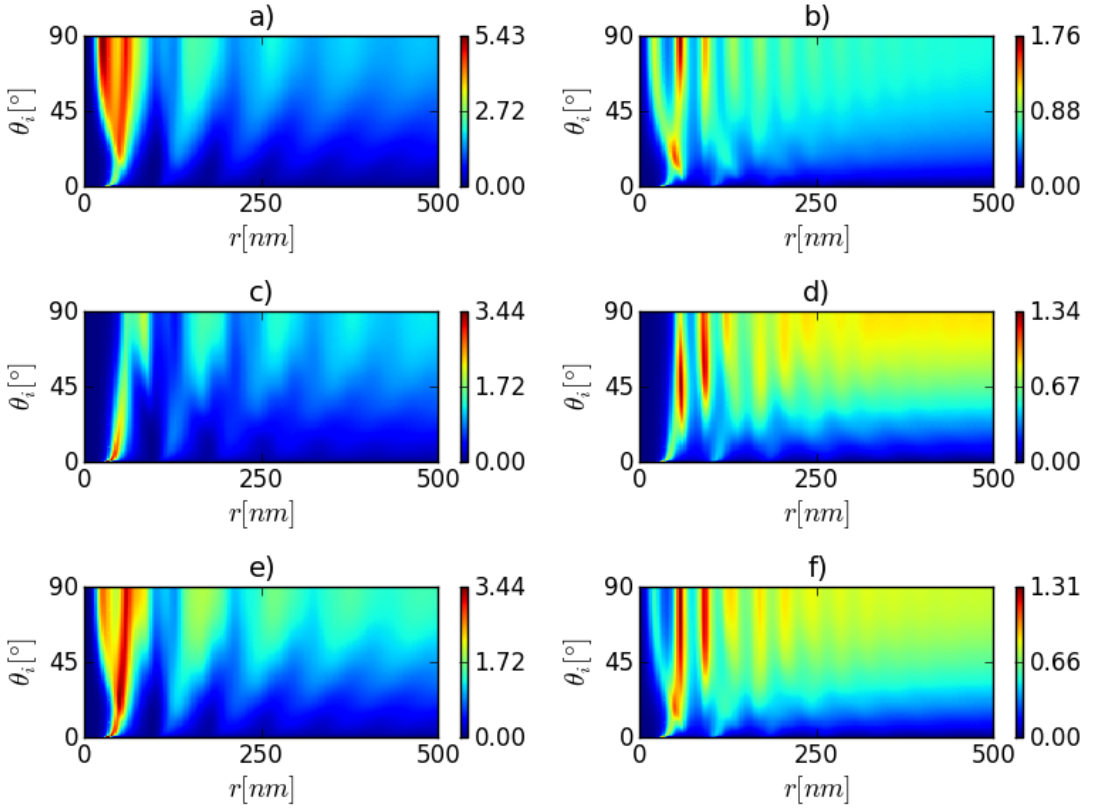

Figure 5.2: Simulated scattering (left part of figure) and absorption (right part of figure) efficiencies as function of radius r and incident angles θ_i. Light is illuminated at a wavelength λ of 600 nm. a) Scattering efficiency for p-polarised light. b) Absorption efficiency for p-polarised light. c) Scattering efficiency for s-polarised light. b) Absorption efficiency for s-polarised light. a) Scattering efficiency for unpolarised light. b) Absorption efficiency for unpolarised light.

Scattering and absorption efficiencies as function of radius and incidence angle

From Figure 5.2 we can observe that both scattering and absorption efficiencies are zero for small incidence angles, due to light illumination nearly parallel to the cylinder axis. For certain radii the absorption efficiencies are not very sensitive to the incident angle. They are nearly constant, due to the lowest orders of the resonance modes join each others and contribute with the cylinder axis. This is very promising for photovoltaic components, such as solar cells where it is beneficial to absorb light in as broad range of incident angles as possible. This also imply that some specific radii are more beneficial for making photovoltaic applications than others.

Scattering and absorption efficiencies as function of incidence angle and wavelength

Since there is a natural symmetry between incident angles of 0°-90° and from 90°-180°, due to the cylinder geometry, Figure 5.3 is displayed for angles between 0° and 90°. The

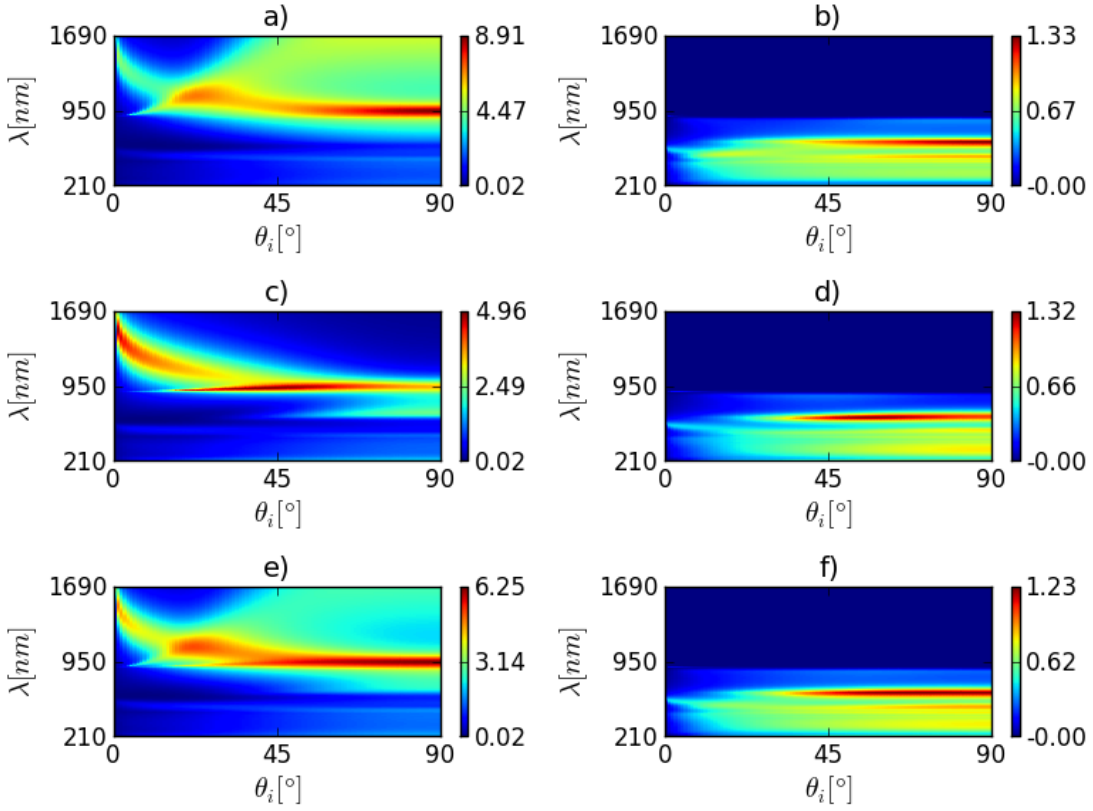

Figure 5.3: Simulated scattering (left part of figure) and absorption (right part of figure) efficiencies as function of incident angles θ_i and wavelength λ. The radius r of the nanowire is set to 100 nm. a) Scattering efficiency for p-polarised light. b) Absorption efficiency for p-polarised light. c) Scattering efficiency for s-polarised light. b) Absorption efficiency for s-polarised light. a) Scattering efficiency for unpolarised light. b) Absorption efficiency for unpolarised light.

band gap wavelength can easily be observed at $\lambda = 873$ nm. For longer wavelengths, the absorption efficiencies become zero, while the scattering efficiencies increase abruptly. At small angles, where light is illuminated parallel with the cylinder axis the absorption efficiencies are zero. For angles around 45°, and higher, we can observe an increase in the absorption efficiencies, and small differences in these values.

5.1.2 Simulations of specular reflectance using effective medium theory

The simulated specular reflectance for ensembles of nanowires are simulated as function of wavelength λ and incidence angle θ_i. All Mueller matrix elements are normalised to M_{11}. The input values used in the simulations was decided from cross-section SEM measurements. These input values are based on average values of the radius, length and distance in between the nanowires measured several places across the samples, summarized in Table 4.1. For establishing more accurate input values it should be considered to calculate the geometrical quantities from probability density functions using curve fitting, instead of using average values.

The amount of particles per unit area, N is calculated for the density of nanowires along the 111-direction, across the substrate. In the SEM images, in particular Figure 4.7, it can be spotted that not all nanowires are laying in the 111-direction but some have been broken and lay nonvertically during growth process. These nonvertical nanowires result in lower density, which give a inconsistency value for the calculation of N. A more accurate way to estimate the density of nanowires would be through counting all the nonvertical and all vertical nanowires an estimate the density through the volume filling fraction for the nanowire material.

For random growth ensembles of nanowires it was very difficult to determine exact distance between the nanowires, since this distance vary a lot across the sample. Some neighbouring nanowires could lay very close to each other, while some could lay very far between each other. This can be seen in Figure 4.8 and Figure 4.6. Therefore it became difficult to estimate a suitable value for the amount of particles per unit area N, and therefore also difficult to find a simulation that correspond exactly to the measurement sample.

Long random nanowires (SC507)

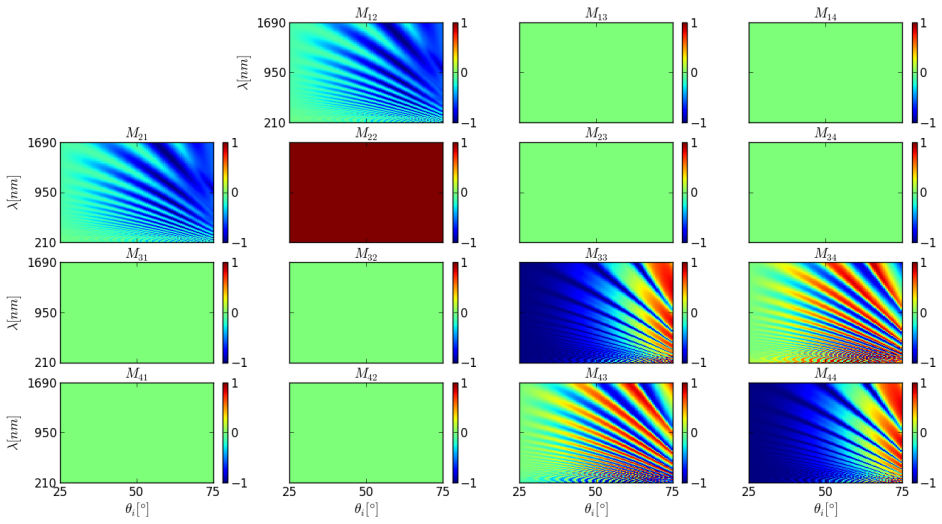

Figure 5.4: Simulated Mueller matrix of specular reflectance for random growth nanowires. The data are represented in a color map plot. The length of the nanowires are set to 3.8 μm, while the distance between the nanowires are 0.6 μm. The nanowires consist of pure GaAs with a radius of 50 nm.

Figure 5.4 shows the simulated specular reflectance for a random growth high density nanowire sample, as a function of incidence angle θ_i and wavelength λ, corresponding to sample SC507. The radius was set to 50 nm, the height to 3.8 μm, and distance between the samples to be 0.6 μm. The off-block-diagonal elements are all zero corresponding to an isotropic Mueller matrix, similar to equation (3.27). The Mie resonance modes can be observed for the block-diagonal elements, except for M_{22}. At short wavelength, under the band gap wavelength of GaAs, the resonance modes interact with each other resulting in numerical noise. In Figure 5.4 can we observe that the amplitudes decrease toward zero

for decreasing incidence angles, while increasing wavelength increase the distance between the resonance modes.

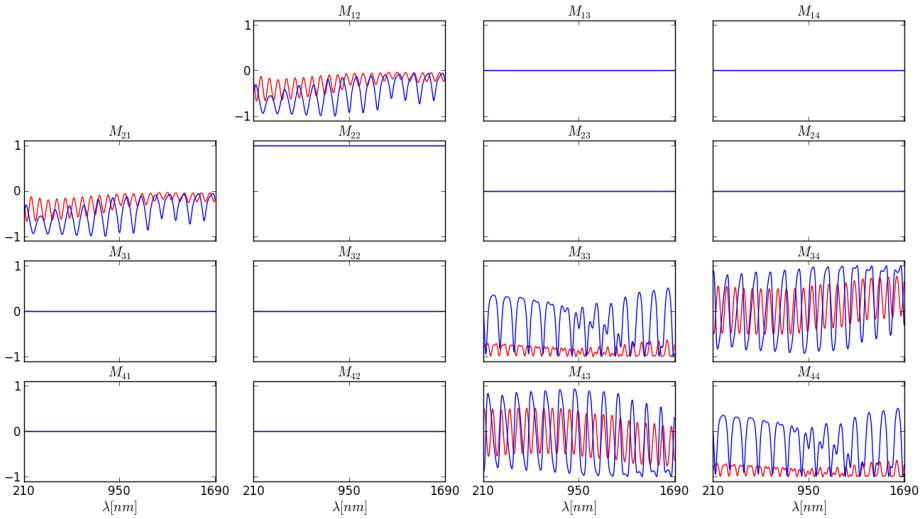

Figure 5.5: Simulated Mueller matrix of specular reflectance for random growth nanowires. The red solid line represent the incident angle of 45°, while the blue solid line represent the incident angle of 65°. The length of the nanowires are set to 3.8 μm, while the distance between the nanowires are 0.6 μm. The nanowires consist of pure GaAs with a radius of 50 nm. Since the Mueller matrix is isotropic some elements have similar values independent of incident angle and only the blue line is visible in the Figure.

For easier comparison with simulations was the simulated spectroscopic Mueller matrix plotted as a function of wavelength for a given incidence angle of 45° (red lines in Figure 5.5) and 65° (blue lines in Figure 5.5). In Figure 5.5 it is possible to observe the characteristic oscillations for the block-diagonal elements (except for M_{22}) for both incidence angles. We can observe smaller amplitudes, but more frequent oscillations, for the incident angle of 45° compared to an incident angle of 65°.

Figure 5.6 shows the real and imaginary components to the calculated effective refractive index as a function of wavelength for p- and s-polarised light. The red line represent the effective refractive index for s-polarised light, while the blue line represent the effective refractive index p-polarised. For long wavelength we can observe the effective refractive index to become similar for p- and s-polarised light. The real components are close to one, which is beneficial for broadband and light coupling. The imaginary components are close to zero.

Positioned core-shell nanowires(SC571)

Figure 5.7 shows the simulated specular reflectance for core-shell positioned nanowires. These nanostructures consist of a shell of GaAs with a radius of 100 nm from the cylinder center, and a shell of $Al_{0.3}Ga_{0.7}As$ with a radius of 170 nm from cylinder center. These radii were estimated from growth time ratios between the thicknesses of the core and the shell. This gave an inaccurate estimation of a core of 100 nm and a shell thickness of 35

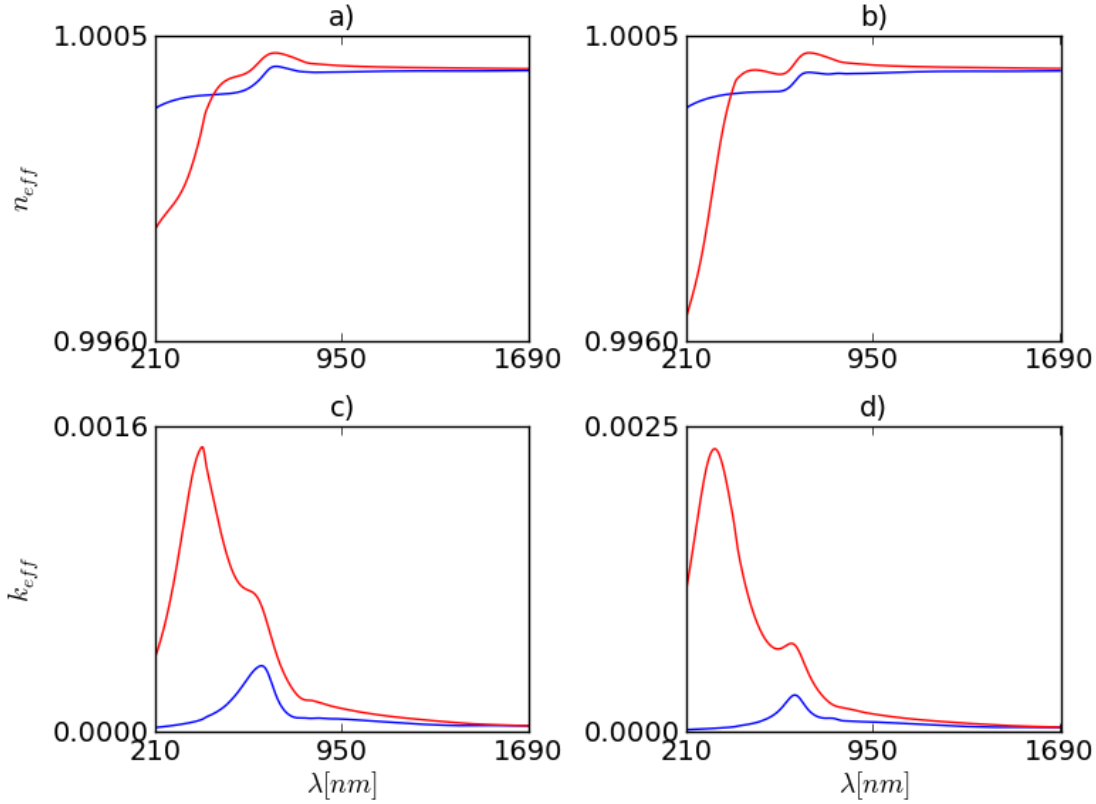

Figure 5.6: Calculated effective refractive index for p- and s-polarised light as function of wavelength λ for incidence angles of 45° (a) and c)) and 65° (b) and d)). The red solid line represent the effective refractive index for s-polarised light, while the blue solid line represent the incident angle for p-polarised light. The length of the nanowires are set to 3.8 μm, while the distance between the nanowires are 0.6 μm. The nanowires consist of pure GaAs with a radius of 50 nm.

nm around the core. The length of the wires was set to be 3.1 μm, and since these wires are positioned grown, the distance between the nanowires are fixed to 1.0 μm. Still we can observe simulations of an isotropic Mueller matrix. There are larger differences in the amplitudes of the block-diagonal elements, and the resonance modes are more difficult to detect compared to the resonance modes for core nanowires, Figure 5.4.

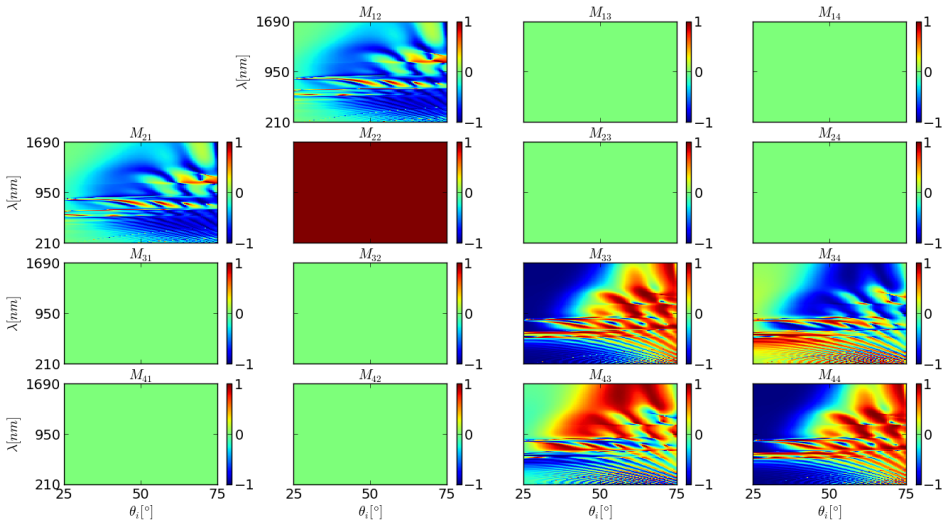

Figure 5.7: Simulated Mueller matrix of specular reflectance for positioned grown core-shell nanowires. The data are represented in a color map plot. The length of the nanowires are set to 3.1 μm, while the distance between the nanowires are 1.0 μm. The nanowires consist of a core of GaAs with a radius of 100 nm and a shell consisting of AlGaAs with a radius of 170 nm from the center

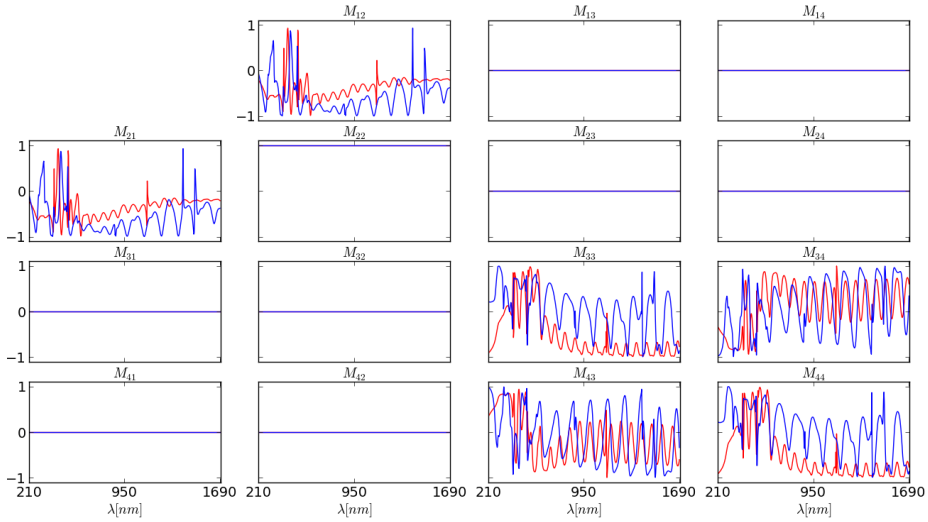

Figure 5.8: Simulated Mueller matrix of specular reflectance for position grown nanowires. The red solid line represent the incident angle of 45°, while the blue solid line represent the incident angle of 65°. The length of the nanowires are set to 3.1 μm, while the distance between the nanowires are 1.0 μm. The nanowires consist of a core of GaAs with a radius of 100 nm and a shell consisting of AlGaAs with a radius of 170 nm from the center. Since the Mueller matrix is isotropic some elements have similar values independent of incident angle and only the blue line is visible in the Figure.

Again is the Mueller matrix displayed as function of wavelength for a given incidence angles

of 45° (red lines in Figure 5.8) and 65° (blue lines in Figure 5.8). It can be observed for a specific wavelength, around the band gap wavelength of GaAs, an abrupt decrease of amplitudes of the oscillations, especially for shorter incidence angles. This can be seen as a separation of the scattering resonance in Figure 5.7, were some resonant modes stop and some new are established. This behaviour is caused by change in complex refractive index between the core and the shell of the nanowires. Still do the resonance modes lay wider in between each other for increasing incidence angles and wavelengths.

In Figure 5.7 it is possible to observe the band gap wavelength for both GaAs and AlGaAs. Since the band gap of $Al_{0.3}Ga_{0.7}As(E_g = 1.796eV)$ are higher than GaAs ($E_g = 1.42eV$), which corresponds to a short wavelength for $Al_{0.3}Ga_{0.7}As$ ($\lambda = 690nm$) than GaAs ($\lambda = 873nm$). This will lead to more amount of light scattering at shorter wavelength for the AlGaAs shell. Above the band gap wavelength of GaAs both core and shell do not absorb light and the scattering increases even more.

5.2 Ellipsometric measurements

By using a J. A. woollam Co. RC2 ellipsometer measurements of the spectroscopic Mueller matrix was preformed as function of wavelength and variation of incidence angles. All measurements included in this thesis are done with focus probes, even though some measurements without focus probes were preformed for comparing the differences in results and accuracy. Pictures, taken with the ellipsometer camera, were helpful for detecting scratches and defects on the substrates, shown in Figure 4.2. It was therefore avoided to do measurements at these areas, since it may lead to inaccurate readings. For curiosity it was preformed some measurements at scratchy areas, which gave far from expected Mueller matrix compared with the measurements on good locations.

There were problems in measuring long nanowires, like sample SC507, because they absorb too much of the illuminated beam and the intensity of the reflected beam became very low. This can become a problem for in situ measurements if the wires become too long, since no light will be detected at a certain length. Thick nanowires, with high radii, as sample SC570 and SC571 was also very difficult to measure, due to the fact that they also absorb too much light. The SEM images do also reveal surface roughness between the substrate and the nanowire layer, which would lead to additional light scattering and reduction in reflection.

Spectroscopic Mueller matrix ellipsometry by varying incident angle (SC507)

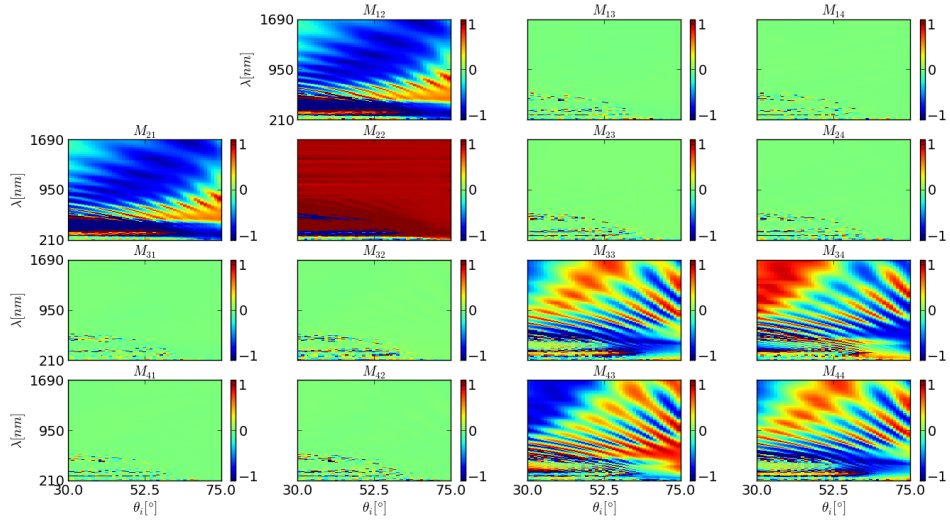

Figure 5.9: Measured Mueller matrix of specular reflectance for random growth nanowires, for sample SC507. The data is represented in a color map plot as function of incidence angle and wavelength. The length of the nanowires was measured to be 3.8 μm, while the distance between the nanowires were 0.6 μm. They consist of pure GaAs with a radius of 50 nm.

The average height of the nanowires for sample SC507 were estimated to be 3.8 μm with a standard deviation of ± 0.3 μm. The radius was estimated to be 52 nm with a standard deviation of ± 7 nm. The average distance between the wires was more difficult to estimate. Since the nanowires were random grown, the distance deviate a lot, an average distance was determined to be 0.6 μm with a deviation of ± 0.2 μm.

From Figure 5.9 we can observe noise for short wavelengths and short incidence angles, due to difficulties in detect high intensities for short incident angles. At wavelength above the band gap wavelength it is possible to detect the resonance modes, similar to the simulated in Figure 5.4.

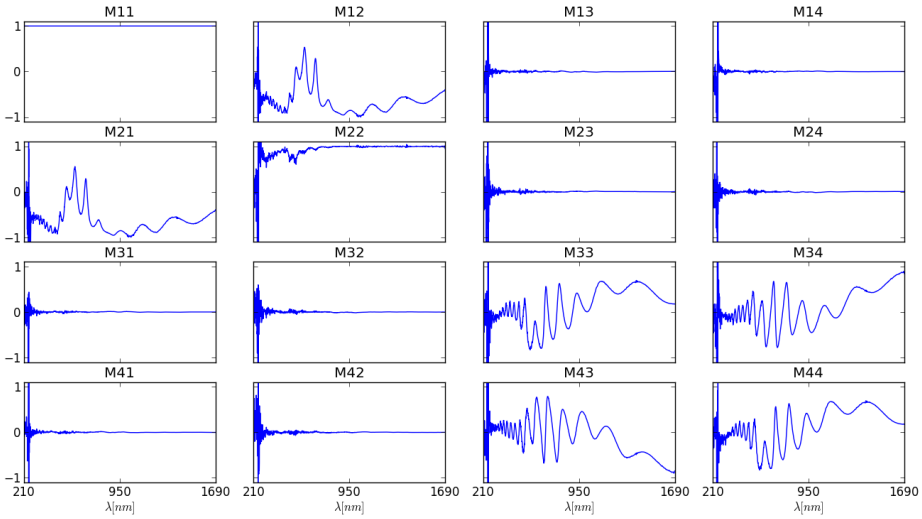

Figure 5.10: Measured Mueller matrix of specular reflectance for random growth nanowires, for sample SC507. The data are plotted for as function of wavelength and for an incident angle of 45° The length of the nanowires was measured to be 3.8 μm, while the distance between the nanowires were 0.6 μm. They consist of pure GaAs with a radius of 50 nm.

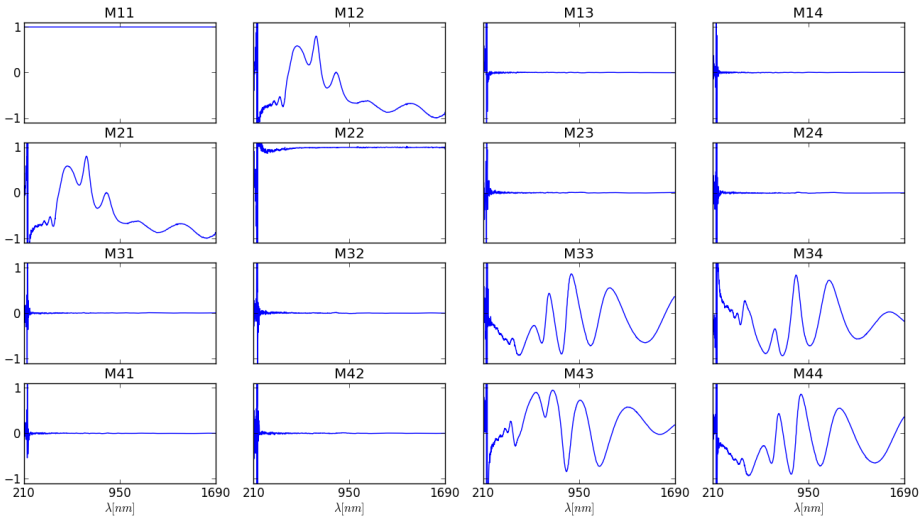

Figure 5.11: Measured Mueller matrix of specular reflectance for random growth nanowires, for sample SC507. The data are plotted for as function of wavelength and for an incident angle of 65° The length of the nanowires was measured to be 3.8 μm, while the distance between the nanowires were 0.6 μm. They consist of pure GaAs with a radius of 50 nm

The measurements are noisy for short wavelength in UV range in Figure 5.10 and Figure 5.11. This is an indication of The characteristic oscillations can be observed in the block diagonal elements for longer wavelength. It is also possible to detect anisotropy in the off-block diagonal elements.

By comparing with simulations in section 5.1.2, there can clearly be observed differences in

amplitudes and frequency of the oscillations for both incident angles. The resonance modes are not similar either. There are some indication of interruption in the measured reflected values. This could be explain due to surface roughness, inaccuracies under growth or measurements, as well as sample defects on measured areas. There are also some weaknesses in the algorithm, that will be discussed later. Since light scattering on a surface occur more easily for shorter wavelengths, it is possible to detect depolarisation in the measured Mueller matrix in Figure 5.10 and Figure 5.11. Small amount of noise can be observed for the shortest wavelength in UV range. This observed noise is caused by the xenon lamp, due to rapid decrease in light intensity in the UV region for high energies [19].

In Figure 4.2 it is possible notice change in beam spot on the sample at changes of incident angles. At 45°the beam is nearly circular(Figure 4.2a) and c)), while for 65°the beam shape has become slightly more elliptical (Figure 4.2b) and d)). For even higher incident angles the beam becomes even more elliptical. The reflected light can clearly be seen to be diffused more for higher incident angles, and may be more difficult to be detected by the detector.

Spectroscopic Mueller matrix ellipsometry by varying incident angle for a core-shell structure (SC571)

Since the nanowires in sample SC571 absorb to much light it was difficult to measure the spectroscopic Mueller matrix shown in Figure 5.12, and the results are not comparable. This was a little disappointing, because it would be interesting to compare the simulated Mueller matrix for a core-shell structure with the measured.

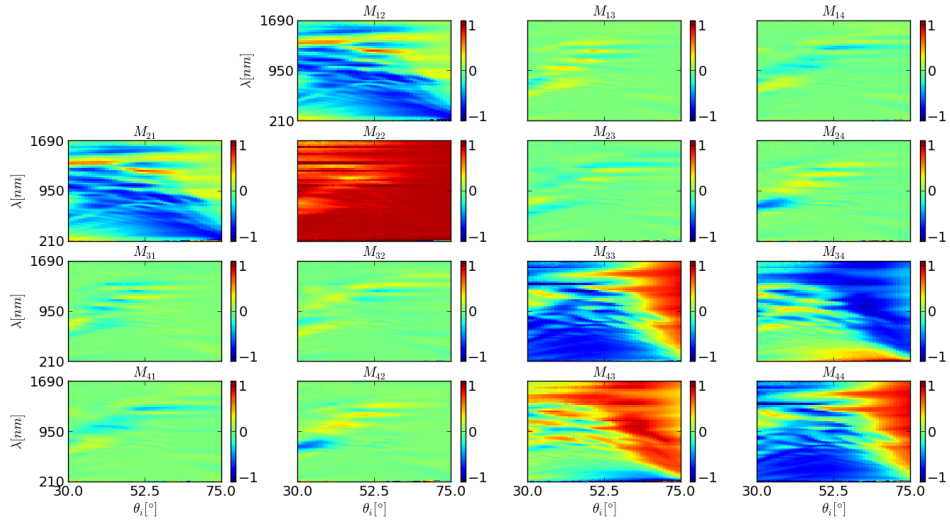

Figure 5.12: Measured Mueller matrix of specular reflectance for position grown core-shell nanowires, for sample SC571. The data is represented in a color map plot as function of incidence angle and wavelength. The length of the nanowires was measured to be 3.1 μm, while the distance between the nanowires were 1.0 μm. They consist of pure GaAs as core material and AlGaAs as shell. The total radius is 168 nm.

5.2.1 Differences between simulations and measurements

Since the nanowires samples show relatively high anisotropy it may be considered to simulate the specular reflectance for an anisotropic Mueller matrix. This may give more equal behaviour and amplitude values for simulated and measured data. SEM measurements gave variations in the geometrical quantities of the nanowires, and therefore it was difficult to estimate a accurate value for the amount of particles per unit area, N. Especially it was difficult to find a suited distance between the wires for random growth samples, but it also clearly possible to see from the SEM images, that the radii and height vary across the sample. The droplet on top of the nanostructures may also be significant.

Since the nanowires are epitaxial grown in different arrangement, such as hexagonal or random, it is difficult to determine the distance between the wires. For hexagonal lattice structures the distance between the wires are around 1 μm. However for a random lattice structure, the distance between the nanowires vary a lot more, some lay very close to each other (about 0.3 μm), but some can lay as far as over 1 μm. This makes it difficult to determine an average distance between the wires.

The simulation assume p-polarised light to propagate in z-direction while s-polarised propagate in x-y direction. This is a terrible assumption for incoming illuminated light at oblique incidence. This assumption lead to wrong values for calculation of the dielectric tensor. The simulation should therefore follow a coordinate system, where the z-direction is aligned dependent on the incident angle, and the substrate with the nanowires should be rotated with respect to the illuminated beam using Euler rotation.

Among others Figure 4.8 and Figure 4.6 it is possible to observe some significant surface roughness, this roughness will affect the reflection measurements of the illuminated beam. This can also give significant changes in amplitude as well as the detection of anisotropy in the Mueller matrix.

Depolarisation of sample is the main reason for measurement errors. The morphology of the sample is therefore important, the more surface roughness, the more depolarised sample, which will experience an increase in measurement errors. There may also exist small errors in the measurement due to bad calibration of sample. Partly polarised light is also more difficult to measure and contribute to an arise in measurement errors. Partly polarised light is generated due to surface roughness and thickness inhomogeneity across the film surface.

The amount of light recorded by the detector do also change for variation in the incident angle. The shape of the beam change and lead to a elliptical shape for increasing incident angle. For high enough angles would more of this reflected beam be diffused away from the detector.

Ideally it should be done calibrations for every incident angle under an incident angle scan for providing the most accurate results. The calibration was only done for one incident angle (65°), which could lead to measurements errors.

Measured spectroscopic Mueller matrix ellipsometry upon change in azimuthal rotation of the sample

For mapping out the symmetry of patterned nanowires, the spectroscopic Mueller matrix was measured as function of azimuthal rotation. The nanowires can be regarded as a two

dimensional photonic crystal with GaAs and air as the alternating dielectric layers. We selected to study the spectroscopic data for a complete loop (0°-360°) with step of 10° and for incidence angles of 45° and 65°. The symmetric features can be observed in Figure 5.14, where we can observe a periodicity of six. This indicates that the nanowires are aligned in a hexagonal lattice structure. For more detailed investigation the sample was also measured for an azimuthal rotation between 0° and 90°, with a step of 2°. This can be seen in Appendix .

The sample SC504 consist of positioned nanowires at a fixed distance of 1.0 μm with a standard deviation of 0.1 μm. The average length was measured to be 1.4 μm with a standard deviation of 0.1 μm. The radius was 58 nm with a deviation of 5 nm.

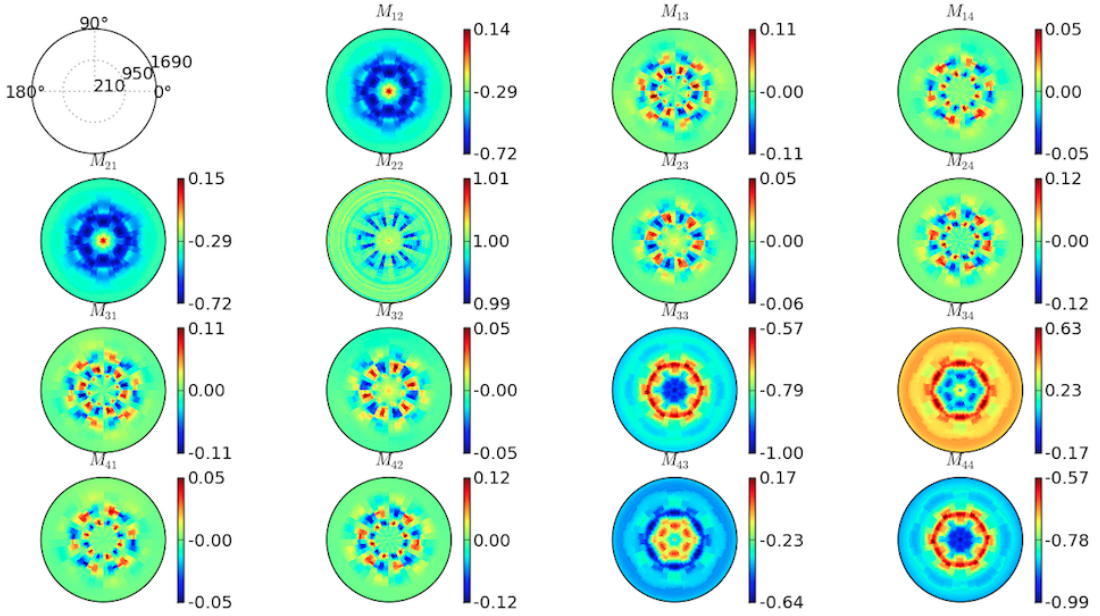

Figure 5.13: Measured spectroscopic Mueller matrix for an incident angle of 45°, and complete azimuthal rotation ϕ of sample SC504 between 0°-360°. The data is presented in a polar color map, where the radius represent the wavelength λ in nm. The data is ranged from 210 nm, at the circle center, to 1690 nm, at the outer edge. The azimuthal rotation is given by the polar angle. The beam position is shown in Figure 4.2a) and c).

There were some problems measuring the substrate for rotating angles due to some significance differences between 0° and 180°. Therefore measurements on an isotropic silicon wafer was done to check the validity of the measurements. This show minimal differences for the Mueller matrix for difference in the azimuthal rotation angle between 0° and 180°.

Even though the off-block-diagonal elements are significantly smaller than the block-diagonal elements in Figure 5.13 and A.4, it is clearly posible to observe some anisotropy in the samples. This contradicts the assumption of an isotopic material for the simulated Mueller matrix.

A periodicity of six for a complete loop of azimuthal rotation correspond to a periodicity of 60 degrees. By looking at SEM pictures and calculating degrees and length between the nanowires it is possible to detect a hexagonal pattern. It is also possible to detect a hexagonal lattice from the Fourier power spectra. The power density spectra for sample

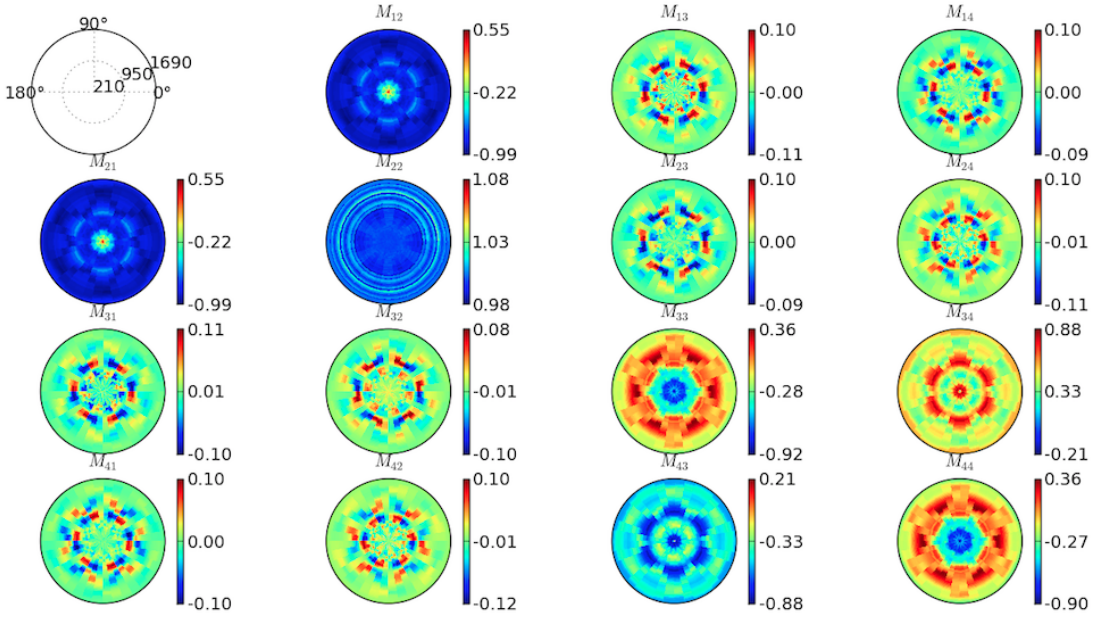

Figure 5.14: Measured spectroscopic Mueller matrix for an incident angle of 65°, and complete azimuthal rotation ϕ of sample SC504 between 0°-360°. The data is presented in a polar color map, where the radius represent the wavelength λ in nm. The data is ranged from 210 nm, at the circle center, to 1690 nm, at the outer edge. The azimuthal rotation is given by the polar angle. The beam position is shown in Figure 4.2b) and d).

SC571 is shown in Figure 4.3. We can observe a hexagonal symmetry with some disorder in the lattice. The power spectra for SC504 show even more disorder (this power spectra is not included in the thesis). From Figure 4.7 it can be spotted many fallen nanowires. The nanowires are also grown in very low density. This gave problems in measuring the incidence angles, and the reflection from substrate dominate these measurements.

It is possible to detect the rayleigh anomalies phenomena for the periodic grating structures in Figure 5.13 and Figure 5.13. This phenomena observed due to the holes, were the nanowires are grown out of, and not the nanowires themselves. From the SEM pictures, Figure 4.7 we can see that the nanowires are grown at very low density. The incidence angle measurements reveal also poor measurements, with few oscillations. By add a model of the under layered substrate it can be shown that the substrate is reflected more than the nanowires.Even so the azimuthal rotation show a nice and periodic grating.

6. Conclusion

In this thesis we have modulate the specular reflectance for illuminated light at oblique incidence for an ensemble of nanowires with effective medium theory, for single nanowires and for core-shell structures.

By comparing simulated Mueller matrix, based on cylinder scattering and effective medium theory, with measured spectroscopic Mueller matrix it is possible to detect similar behaviour, although anisotropy is observed. There are major differences between the values of measured and simulated data. This could be due to variations in geometrical quantities of the wires, which makes it difficult to estimate a good value for the amount of particles per unit area. A more precise way would maybe be to estimate the density through the volume filling fraction, which also distinguish between fallen and vertically grown nanowires.

There is a weakness in the simulations, since ϵ_p is assumed to be in the z-direction and ϵ_s in the x-y direction, even for an oblique incidence light wave. An improved effective medium model is therefore necessary.

Even so the possibilities of modelling the nanowires based on effective medium theory, with a corresponding scattering matrix, looks like a good assumption, which can further be used for in situ characterization. A problem occur when the nanowires become too long or too thick, and they absorb too much light, and give inaccurate measurements.

For the investigation of positioned growth nanowires, it is possible to detect a high amount of anisotropy for the samples, even for samples with low density of nanowires. This show that the small correction in calculation of an isotropic Mueller matrix, in the algorithm, deviate more than expected.

6.1 Future work

For the computer simulations of the Mueller matrix it would be interesting to extend the program such that the algorithm not only calculate the Mueller matrix for an isotropic medium, where the off-block-diagonal elements are zero, but in fact calculate the anisotropic Mueller matrix. Even though this is a small correction, measurements show that the nanowire sample are anisotropic and therefore should be compared with anisotropic simulation instead of the isotropic.

It should also be made an ellipsometric data model in the complete ease software for fitting the experimental data as close as possible with simulations. The data model should be based on the simulations of effective medium theory and corresponding effective refractive indexes. This would be in great value for easier understanding the interpretation of the

measured spectroscopic Mueller matrix as well as possibilities for in-situ measurements of nanowire growth.

Bibliography

[1] A. R. Barron. Molecular beam epitaxy. `http://cnx.org/contents/1096167b-8518-4159-a88d-3b2ae4df6645:28/Chemistry_of_Electronic_Materi`. Sourced: 9.12.2014.

[2] H Junghwan. Introduction to e-beam lithography. Presented in TFE4575, NTNU, 2014.

[3] M. Bruno G. Cattelan D Cobet C. Martino A. Fleischer K. Dohcevic-Mitrovic Z. Esser N. Galliet M. Gajic R. Losurdo, M. Bergmair, K. Humlicek J. Ossikovski R. Popovic Z. V. Hemzal, D. Hingerl, and O. Saxl. Spectroscopic ellipsometry and polarimetry for materials and systems analysis at the nanometer scale: state-of-the-art, potential, and perspectives. *Journal of Nanoparticle Research*, 11:1521–1554, 2009.

[4] RS Wagner and WC Ellis. *Vapor-liquid-solid mechanism of crystal growth and its application to silicon*. Bell Telephone Laboratories, 1965.

[5] G. E. Cirlin, V. G. Dubrovskii, Yu. B. Samsonenko, A. D. Bouravleuv, K. Durose, Y. Y. Proskuryakov, Budhikar Mendes, L. Bowen, M. A. Kaliteevski, R. A. Abram, and Dagou Zeze. Self-catalyzed, pure zincblende gaas nanowires grown on si(111) by molecular beam epitaxy. *Phys. Rev. B*, 82:035302, Jul 2010.

[6] Linus C. Chuang, Michael Moewe, Chris Chase, Nobuhiko P. Kobayashi, Connie Chang-Hasnain, and Shanna Crankshaw. Critical diameter for iii-v nanowires grown on lattice-mismatched substrates. *Applied Physics Letters*, 90(4):–, 2007.

[7] White J. S. Park J. Schuller J. A. Clemens B. M. Cao, L. and Brongersma M.L. Engineering light absorption in semiconductor nanowire devices. *Nature materials*, 5.7.2009.

[8] Jahr N. Leiterer C. Csáki A. Fritzsche W. Bronstrup, G. and S. Christiansen. Optical properties of individual silicon nanowires for photonic devices. *ACS nano*, 4(12):7113–7122, 2010.

[9] G. Grzela. *Directional Light Emission and Absorption by Semiconductor Nanowires*. PhD thesis, Eindhoven University of Technology, 2013.

[10] Grzegorz Grzela, Djamila Hourlier, and Jaime Gómez Rivas. Polarization-dependent light extinction in ensembles of polydisperse vertical semiconductor nanowires: A mie scattering effective medium. *Phys. Rev. B*, 86:045305, Jul 2012.

[11] Yaoguang Ma, Xin Guo, Xiaoqin Wu, Lun Dai, and Limin Tong. Semiconductor nanowire lasers. *Adv. Opt. Photon.*, 5(3):216–273, Sep 2013.

[12] Katsuhiro Tomioka, Junichi Motohisa, Shinjiroh Hara, Kenji Hiruma, and Takashi Fukui. Gaas/algaas core multishell nanowire-based light-emitting diodes on si. *Nano Letters*, 10(5):1639–1644, 2010. PMID: 20377199.

[13] Fang Qian, Silvija Gradečak, Yat Li, Cheng-Yen Wen, and Charles M. Lieber. Core/multishell nanowire heterostructures as multicolor, high-efficiency light-emitting diodes. *Nano Letters*, 5(11):2287–2291, 2005. PMID: 16277469.

[14] A.R. Gobat, M.F. Lamorte, and G.W. McIver. Characteristics of high-conversion-efficiency gallium-arsenide solar cells. *Military Electronics, IRE Transactions on*, MIL-6(1):20–27, Jan 1962.

[15] R. R. LaPierre. Numerical model of current-voltage characteristics and efficiency of gaas nanowire solar cells. *Journal of Applied Physics*, 109(3):–, 2011.

[16] Anna Dalmau-Mallorqui Martin Heiss and Anna Fontcuberta i Morral.

[17] K. Vedam. Spectroscopic ellipsometry: a historical overview. *Thin Solid Films*, 313–314(0):1 – 9, 1998.

[18] H. G. Tompkins and E. A. Irene. *Handbook of Ellipsometry*. William Andrew, Inc., 2005.

[19] H. Fujiwara. *Spectroscopic Ellipsometry: Principles and Applications*. John Wiley & Sons, Ltd., 2007.

[20] A. Laskarakis, S. Logothetidis, E. Pavlopoulou, and M. Gioti. Mueller matrix spectroscopic ellipsometry: formulation and application. *Thin Solid Films*, 455–456(0):43 – 49, 2004.

[21] Mukesh Ranjan, Thomas W. H. Oates, Stefan Facsko, and Wolfhard Mller. Optical properties of silver nanowire arrays with 35 nm periodicity. *Opt. Lett.*, 35(15):2576–2578, Aug 2010.

[22] Thomas W. H. Oates, Mukesh Ranjan, Stefan Facsko, and Hans Arwin. Highly anisotropic effective dielectric functions of silver nanoparticle arrays. *Opt. Express*, 19(3):2014–2028, Jan 2011.

[23] I. S. Nerbø, S. Le Roy, M. Foldyna, M. Kildemo, and E. Søndergård. Characterization of inclined gasb nanopillars by mueller matrix ellipsometry. *Journal of Applied Physics*, 108(1), 2010.

[24] Ingar Stian Nerbø, Sebastien Le Roy, Martin Foldyna, Elin Søndergård, and Morten Kildemo. Real-time in situ mueller matrix ellipsometry of gasb nanopillars: observation of anisotropic local alignment. *Opt. Express*, 19(13):12551–12561, Jun 2011.

[25] L.M.S. Aas, M. Kildemo, Y. Cohin, and E. Søndergård. Determination of small tilt angles of short gasb nanopillars using uv-visible mueller matrix ellipsometry. *Thin Solid Films*, 541(0):97 – 101, 2013. Current Trends in Optical and X-Ray Metrology of Advanced Materials for Nanoscale Devices {III}.

[26] Lars Martin Sandvik Aas, Morten Kildemo, Christian Martella, Maria Caterina Giordano, Daniele Chiappe, and Francesco Buatier de Mongeot. Optical properties of biaxial nanopatterned gold plasmonic nanowired gridpolarizer. *Opt. Express*, 21(25):30918–30931, Dec 2013.

[27] Z. Ghadyani, M. Kildemo, L. M. S. Aas, Y. Cohin, and E. Søndergård. Anisotropic plasmonic cu nanoparticles in sol-gel oxide nanopillars studied byspectroscopic mueller matrix ellipsometry. *Opt. Express*, 21(25):30796–30811, Dec 2013.

[28] M. Quirk and J. Serda. *Semiconductor Manufacturing Technology*. Prentice-Hall, Inc., 2001.

[29] Stephen Y. Chou, Peter R. Krauss, and Preston J. Renstrom. Nanoimprint lithography. *Journal of Vacuum Science & Technology B*, 14(6), 1996.

[30] C. F. Bohren and D. R. Huffman. *Absorption and Scattering of Light by Small Particles*. Wiley Science Paperback Series, 1998.

[31] C. Safko J. Goldstein, H. Poole. *Classical Mechanics*. Addison Wesley, 2001.

[32] H.C. van de Hulst. *Light Scattering by Small Particles*. Dover Publications, Inc., 1998.

[33] G. E. Jellison. *Handbook of Ellipsometry*. William Andrew, Inc., 2005.

[34] H. Fujiwara. *Spectroscopic Ellipsometry: Principles and Applications*. John Wiley & Sons, Ltd., 2007.

[35] J. J. Gil and E. Bernabeu. Depolarization and polarization indices of an optical system. *Optica Acta: International Journal of Optics*, 33(2):185–189, 1986.

[36] R. A. Chipman. Depolarization index and the average degree of polarization. *Appl. Opt.*, 44(13):2490–2495, May 2005.

[37] D. W. Berreman. Optics in stratified and anisotropic media: 4×4-matrix formulation. *Journal of the Optical Society of America*, 62(4):502–510, 1972.

[38] M. Schubert. *Handbook of Ellipsometry*. William Andrew, Inc., 2005.

[39] S. Robinson and R. Nakkeeran. Photonic crystal ring resonator based optical filters. 2013.

[40] I. Gurwich, N. Shiloah, and M. Kleiman. The recursive algorithm for electromagnetic scattering by tilted infinite circular multilayered cylinder. *Journal of Quantitative Spectroscopy and Radiative Transfer*, 63(2):217–229, 1999.

[41] L. M. S. Aas. *Mueller Matrix Imaging and Spectroscopy*. PhD thesis, Norwegian University of Science and Technology, 2013.

A. Additional measurements

This section of the appendix contain results from the remaining samples, which are not displayed and discussed in the result and discussion chapter of this thesis.

A.1 SC504

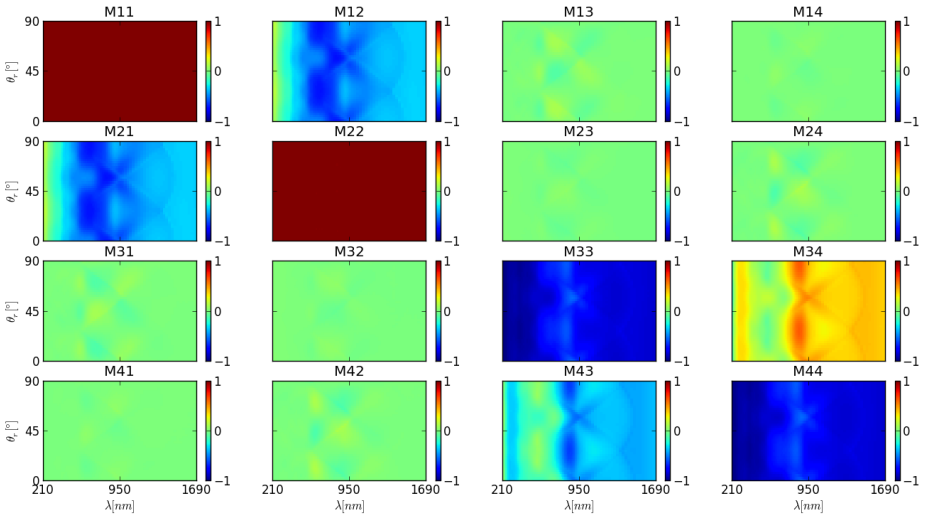

Figure A.1: The measured spectroscopic Mueller matrix for an incident angle of 45°, and an azimuthal rotation of the sample between 0°-90°.The beam position is shown in Figure 4.2a) and b).

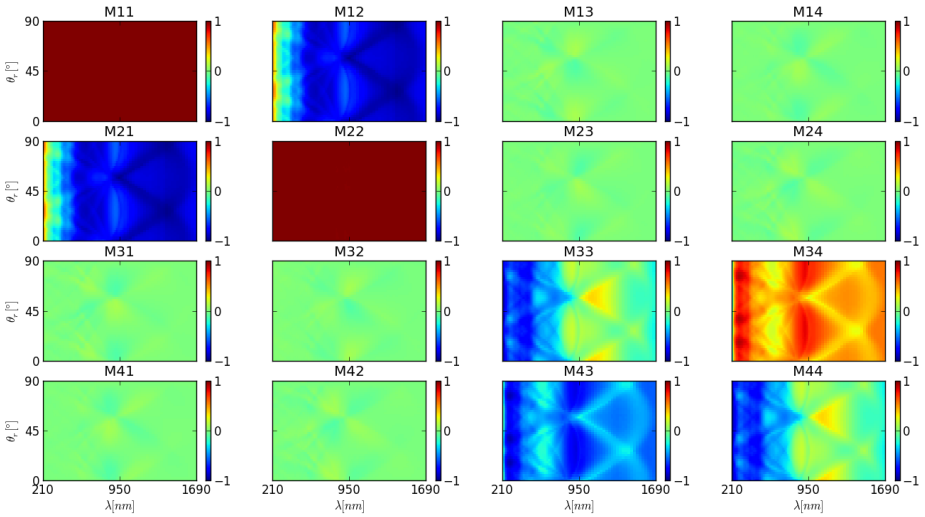

Figure A.2: The measured spectroscopic Mueller matrix for an incident angle of 65°, and an azimuthal rotation of the sample between 0°-90°. The beam position is shown in Figure 4.2c) and d).

Sample SC504 is a positioned grown sample consisting of pure GaAs nanowires with a measured length of 1.4 ± 0.1 μm, radius 58 ± 5 nm and a distance 1.0 ± 0.1 μm.

A.2 SC538

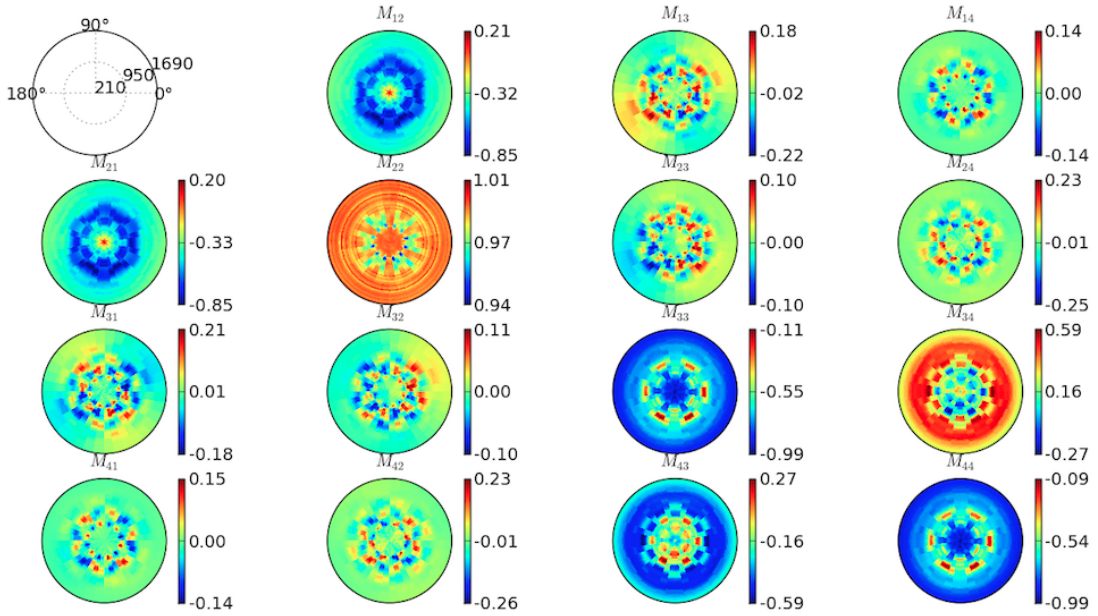

Figure A.3: Measured spectroscopic Mueller matrix for an incident angle of 45°, and complete azimuthal rotation ϕ of sample SC538 between 0°-360°. The data is presented in a polar color map, where the radius represent the wavelength λ in nm. The data is ranged from 210 nm, at the circle center, to 1690 nm, at the outer edge. The azimuthal rotation is given by the polar angle.

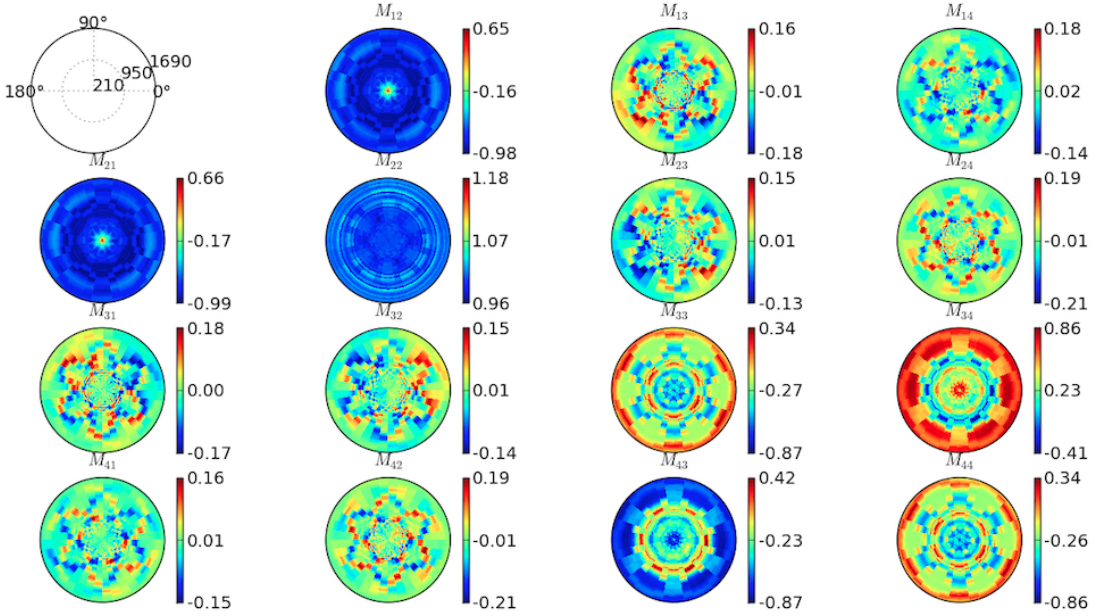

Figure A.4: Measured spectroscopic Mueller matrix for an incident angle of 65°, and complete azimuthal rotation ϕ of sample SC538 between 0°-360°. The data is presented in a polar color map, where the radius represent the wavelength λ in nm. The data is ranged from 210 nm, at the circle center, to 1690 nm, at the outer edge. The azimuthal rotation is given by the polar angle.

Sample SC538 is a positioned grown core-shell sample consisting of GaAs int the core and GaAsSb in the shell. The length was measured to be 2.3 ± 0.1 μm, radius 69 ± 6 nm and a distance 0.9 ± 0.1 μm.

A.3 SC560

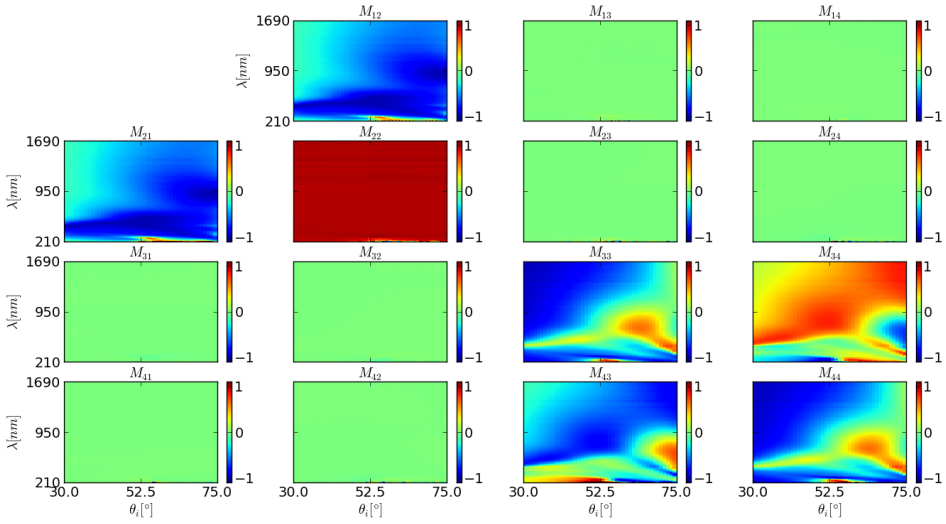

Figure A.5: Measured Mueller matrix of specular reflectance for random growth nanowires, for sample SC560. The data is represented in a color map plot as function of incidence angle and wavelength.

Sample SC560 is a random grown sample consisting of pure GaAs nanowires with a measured length of 0.7 ± 0.1 μm, radius 32 ± 4 nm and a distance 0.3 ± 0.1 μm.

A.4 SC570

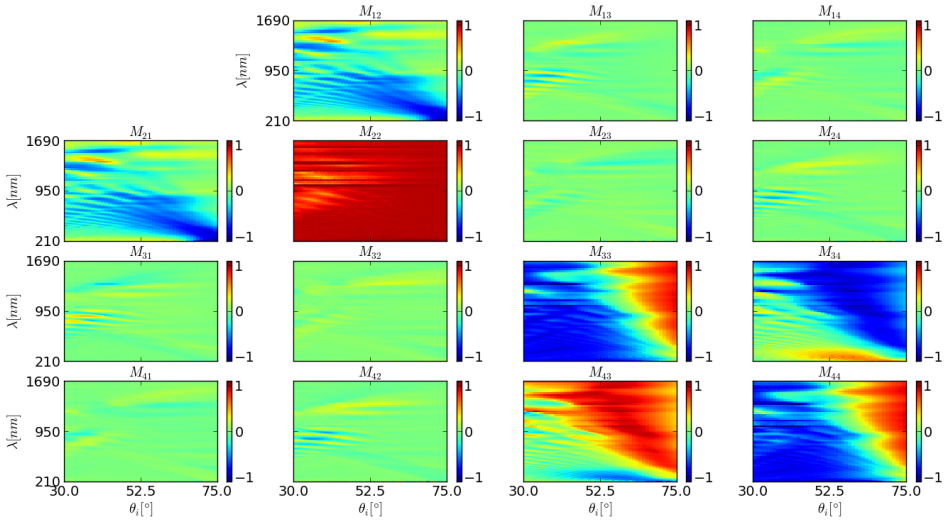

Figure A.6: Measured Mueller matrix of specular reflectance for random growth nanowires, for sample SC560. The data is represented in a color map plot as function of incidence angle and wavelength.

Sample SC570 is a positioned grown sample consisting of pure GaAs nanowires with a measured length of 3.2 ± 0.1 μm, radius 198 ± 13 nm and a distance 1.0 ± 0.1 μm.